Carbon geochemistry of the Atlantis Massif (IODP Expedition 357): Implications for carbonation of mantle peridotites

Lotta Ternieten[1], Gretchen L. Früh-Green[1], and Stefano M. Bernasconi[2]

[1]ETH Zurich
[2]ETH-Zurich

November 21, 2022

Abstract

The carbon geochemistry of serpentinized peridotites and gabbroic rocks recovered during IODP Expedition 357 on the Atlantis Massif (AM) was examined to characterize carbon sources and the fate of dissolved organic (DOC) and inorganic carbon (DIC) in seawater during long-lived hydrothermal circulation and serpentinization. Carbon isotopes reveal three stages of carbonate formation, starting at least 38,000 yr ago: (1) Early dispersed carbonate precipitation, with low water/rock ratios and high temperatures (50 to 190°C); (2) carbonate vein formation related to high and focused fluid fluxes still at higher temperatures (30 to 190°C); and (3) seawater circulation leading to cold carbonate precipitation controlled by late, brittle fractures during uplift and unroofing of the oceanic core complex. Our study reveals three main DIC sources in the system: (1) DIC from abiotic hydrothermal degradation of dissolved organic matter; (2) DIC from seawater; and (3) DIC from mantle-derived volatiles. Basement rocks containing dispersed carbonates are characterized by high concentrations (~800 ppm) of total organic carbon (TOC) and 13C-depleted carbonates. We propose that high seawater fluxes in the southern part of the AM likely favour the transport and incorporation of marine dissolved organic carbon in serpentinites and that carbonates record isotopic signals of organic matter decay. Our study indicates that organic carbon accounts for a significant proportion of the total carbon stored in the Atlantis Massif and suggests that serpentinites may be an important sink of DOC from seawater.

Carbon geochemistry of the Atlantis Massif (IODP Expedition 357): Implications for carbonation of mantle peridotites

Lotta Ternieten[1], Gretchen. L. Früh-Green[1], Stefano M. Bernasconi[1]

[1]Department of Earth Science, ETH Zurich, Clausiusstrasse 25, 8092, Zurich, Switzerland.

Corresponding author: Lotta Ternieten (lotta.ternieten@erdw.ethz.ch)

Key Points:

- Serpentinization is associated with dispersed carbonate and multiple generations of veins formed at temperatures from 7° to 190°C.
- The system has multiple carbon sources: inorganic and organic carbon from seawater, mantle-derived carbon, and minor *in-situ* production.
- Abiotic hydrothermal degradation of dissolved organic matter contributes to carbon cycling in peridotite-hosted hydrothermal systems.

Abstract

The carbon geochemistry of serpentinized peridotites and gabbroic rocks recovered during IODP Expedition 357 on the Atlantis Massif (AM) was examined to characterize carbon sources and the fate of dissolved organic (DOC) and inorganic carbon (DIC) in seawater during long-lived hydrothermal circulation and serpentinization. Carbon isotopes reveal three stages of carbonate formation, starting at least 38,000 yr ago: (1) Early dispersed carbonate precipitation, with low water/rock ratios and high temperatures (50 to 190°C); (2) carbonate vein formation related to high and focused fluid fluxes still at higher temperatures (30 to 190°C); and (3) seawater circulation leading to cold carbonate precipitation controlled by late, brittle fractures during uplift and unroofing of the oceanic core complex. Our study reveals three main DIC sources in the system: (1) DIC from abiotic hydrothermal degradation of dissolved organic matter; (2) DIC from seawater; and (3) DIC from mantle-derived volatiles. Basement rocks containing dispersed carbonates are characterized by high concentrations (~800 ppm) of total organic carbon (TOC) and ^{13}C-depleted carbonates. We propose that high seawater fluxes in the southern part of the AM likely favour the transport and incorporation of marine dissolved organic carbon in serpentinites and that carbonates record isotopic signals of organic matter decay. Our study indicates that organic carbon accounts for a significant proportion of the total carbon stored in the Atlantis Massif and suggests that serpentinites may be an important sink of DOC from seawater.

1 Introduction

Hydrothermal circulation of seawater through the oceanic crust occurs at such rates that entire volume of the ocean may be cycled through the oceanic crust in less than 20 Myr (German & Von Damm, 2003; Wheat & Mottl, 2004). This high fluid flux, coupled with extensive fluid-rock interaction, has significant consequences for the thermal structure and rheology of the oceanic lithosphere, geochemical budgets of the ocean, and microbial processes within and at the seafloor (e.g., Kelley & Früh-Green, 2001; Lister, 1972; Proskurowski et al., 2006; Wheat & Mottl, 2004). At slow-spreading ridges, hydrated upper mantle rocks (serpentinites) are commonly exposed at the seafloor and constitute highly reactive chemical and thermal systems. Carbon - one of the most important elements on Earth - is stored within the lithosphere in the form of gaseous CO_2 and CH_4 within mineral inclusions or as solid phases such as carbonate and graphite and organic compounds. These may persist in ancient mantle domains over extended periods of time. Previous studies have shown that the speciation, concentration and isotopic composition of carbon in serpentinites can be used to gain information about the chemical and physical conditions of the reservoir and the dominant physical, chemical and/or biological processes in the system (Charlou et al., 2002; Delacour, Früh-Green, Bernasconi, & Kelley, 2008; Kelley et al., 2005; Schwarzenbach et al., 2013; Shanks et al., 1995).

Recent studies provide evidence that microbial life may be sustained within the lithosphere by fluid-mediated chemical reactions that provide utilizable energy resources, implying that the deep subsurface biosphere may be the largest microbial habitat on Earth (Barry et al., 2019; Colman et al., 2017; Fullerton et al., 2019). For example, redox reactions during the formation of serpentine from mantle olivine and pyroxene generate substantial amounts of H_2 (Barnes et al., 1972; Barnes & O'Neil, 1969; McCollom & Bach, 2009; Neal & Stanger, 1983; Thayer, 1966), and may promote abiotic synthesis of CH_4 (Abrajano et al., 1990; Charlou et al., 2010; Etiope & Sherwood Lollar, 2013; McCollom, 2013; Szatmari, 1989; Welhan, 1988). Production of H_2 and CH_4 by serpentinization of mantle rocks has been identified at mid-ocean ridges (Cannat et al., 2010; Kelley et al., 2005; Konn et al., 2015; Welhan & Craig, 1979), as well as on-land (Etiope & Sherwood Lollar, 2013) and in the shallow forearc of subduction zones (Mottl et al., 2003; Ohara et al., 2012). Although serpentinization reactions can lead to the production of fluids with high pH ranging from 9 to 11, depending on temperature, which may limit nutrient and electron acceptor availability (Schrenk et al., 2013), metagenomic studies of serpentinization-fueled, hydrothermal deep-sea

vents and continental fluid seeps provide evidence for microbial H_2 and CH_4 utilization (Brazelton et al., 2012; Curtis et al., 2013; Ohara et al., 2012; Schrenk et al., 2013).

Hydration of mantle peridotites can also be associated with large carbonate deposits. Serpentinization at temperatures below approximately 200 to 250°C produces fluids with high Ca^{2+} concentration and high pH, which can cause carbonate precipitation (e.g., Frost & Beard, 2007; Neal & Stanger, 1985; Palandri & Reed, 2004). Recently, carbonate formation from ultramafic rocks has received considerable attention as a potential means to sequester atmospheric CO_2 and reduce global warming (Kelemen et al., 2011; Seifritz, 1990). Previous studies indicate that 5 – 9% of the rocks exposed along slow- and ultraslow-spreading MOR consist of hydrothermally altered peridotite (Cannat et al., 2010; Carlson, 2001) and Kelemen & Matter (2008) argue that mantle peridotites exposed on land have a high capacity to sequester CO_2. This makes serpentinites a significant but still poorly quantified sink for dissolved inorganic carbon (DIC) and dissolved organic carbon (DOC). However, many findings of hydrothermal carbon species are based on experimental studies of fluids (e.g., Seewald, 2001), and only a few studies are available on the geochemistry of organic (Alt et al., 2012; Delacour, Früh-Green, Bernasconi, Schaeffer, et al., 2008; Früh-Green et al., 2004; Kelley & Früh-Green, 1999) and inorganic carbon in oceanic peridotites (Bach et al., 2011; Coggon et al., 2004; Delacour, Früh-Green, Bernasconi, Schaeffer, et al., 2008; Eickmann et al., 2009; Klein et al., 2015; Schwarzenbach et al., 2013). It remains unclear how and to what extent hydration processes in the upper mantle affect the global carbon cycle on different geological time scales. To address these questions, a better understanding of the fate of carbon within these systems is needed.

Here we present a study of carbon and oxygen isotope geochemistry of basement rocks of the Atlantis Massif (AM) close to the Lost City Hydrothermal Field (LCHF) that were recovered during International Ocean Discovery Program (IODP) Expedition 357 (Früh-Green et al., 2017). The LCHF, located on the southern wall of the Atlantis Massif, is an end-member for serpentinite-hosted, hydrothermally active systems at the slow-spreading Mid-Atlantic Ridge (MAR) and serves as an excellent present-day analogue for fossil serpentinite-hosted hydrothermal systems (e.g., Chenaillet Ophiolite, Lafay et al., 2017 ; Northern Apennine ophiolites, Liguria, Barbieri et al., 1979). It is an off-axis, low-temperature, peridotite-dominated system driven by migration of seawater along deeply penetrating fault systems that leads to hydration and serpentinization of the upper mantle. The LCHF offers a unique opportunity to study the interplay of serpentinization, deformation and transformation of

carbon during unroofing and uplift of the AM and the impact these processes have on habitability for microorganisms. This information helps to better understand the fate of carbon in marine hydrothermal systems and provides constraints on the thermal evolution of the Atlantis Massif. Our study aims at characterizing biogenic and abiogenic processes controlling carbon cycling within the oceanic lithosphere. Recent studies indicate that serpentinization reactions have also likely occurred on Mars and beneath icy oceans on Saturn's moon Enceladus and Jupiter's moon Europa (Ehlmann et al., 2010; Glein et al., 2015; Jones et al., 2018; Sekine et al., 2015). Thus, our research is relevant to understand serpentinizing processes on Earth and other terrestrial bodies in the Solar System.

Below we present detailed geochemical analyses of the inorganic and organic carbon together with radiocarbon ages of the basement rocks of the Atlantis Massif. This data allows us to unravel the complexity of this unique system and discuss the sources and speciation of carbon and the critical roles that fluids and deformation play in regulating long-term storage and global carbon cycling within the hydrated and serpentinized oceanic lithosphere.

2 Geological Setting and Sampling

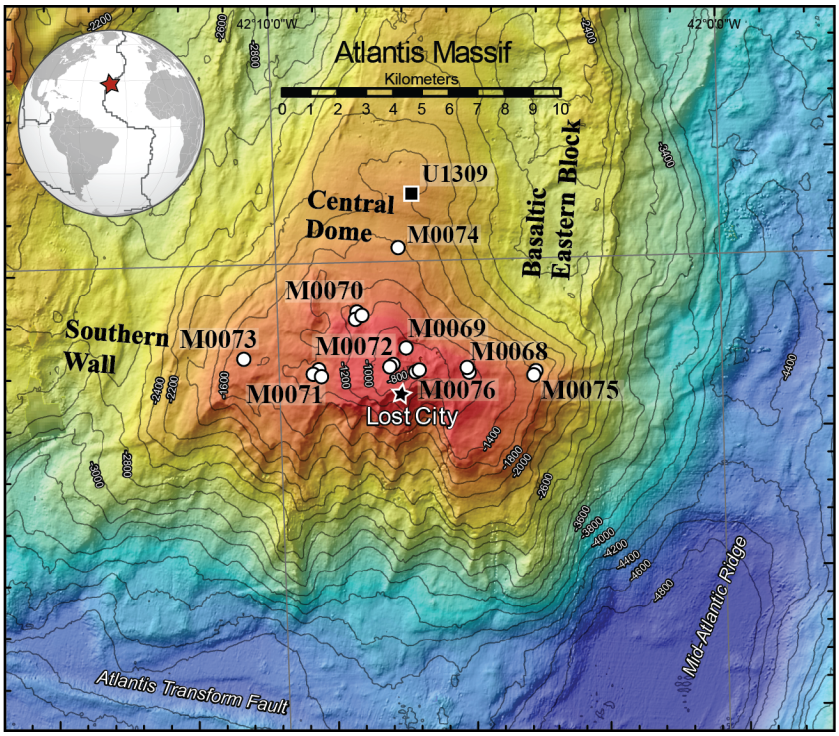

Figure 1. Map of the Atlantis Massif, located at the inside corner of the intersection between the Mid-Atlantic Ridge and the Atlantis Transform Fault, showing the locations of the study

sites (M0068, M0069, M0070, M0071, M0072, M0073, M0074, M0075, M0076) drilled during IODP Expedition 357 (Früh-Green at al., 2017). The black square indicates IODP Site U1309 (IODP Expeditions 304 and 305, Blackman et al., 2006). The black star indicates the location of the Lost City Hydrothermal Field (Kelley et al., 2001).

The Atlantis Massif, located at 30°N along the slow-spreading Mid-Atlantic Ridge (MAR), is a 1.5-2 Myr old, dome-like massif forming the inside corner of the intersection between the MAR and the Atlantis Transform Fault (ATF) (Figure 1). The massif is interpreted as an oceanic core complex (OCC), comprised of lower crustal and upper mantle rocks that were uplifted and exposed by long-lived, low-angle detachment faulting (Blackman et al., 1998, 2002; Cann et al., 1997; Karson et al., 2006). Three lithologic domains can be distinguished: the corrugated central dome comprising mafic rocks ranging from olivine-rich troctolites to oxide gabbros; the variably altered peridotite-dominated southern wall with intermittent mafic plutonic intrusions, which is part of the Southern Ridge and defines the edge of the ATF; and the basaltic eastern block, which is interpreted as the hanging wall of the OCC. The summit peak rises to depths of less than 750 m and is located about midway along the length of the Southern Ridge. The top of the massif is covered by pelagic sediments, rubble, and sedimentary breccias (Blackman et al., 2002; Boschi et al., 2006; Früh-Green et al., 2003; Karson et al., 2006; Schroeder et al., 2002).

The Lost City Hydrothermal Field is located on a fault-bounded terrace just below the top of the southern wall near the summit. It is composed of numerous active and inactive, up to 60 m tall, carbonate-brucite chimneys, which vent low-temperature (40 - 95°C), alkaline (pH 9 - 11) fluids (Kelley et al., 2001, 2005; Lang et al., 2010; Ludwig et al., 2006; Seyfried et al., 2015). The vent fluids are characterized by low silica, metal and CO_2 concentrations and high H_2 (up to 15 mmol/kg), CH_4 (1 – 2 mmol/kg), Ca (~30 mmol/kg), formate (36 – 158 µm/kg), acetate (1 – 35 µmol/kg), and low-molecular-weight hydrocarbons concentrations. The high concentrations of molecular hydrogen, methane, and formate could provide metabolic energy for microbes (Lang et al., 2012; McCollom & Seewald, 2007). Recent genetic sequencing efforts demonstrated that the active carbonate chimney structures at Lost City host microbial communities dominated by archaeal Methanosarcinales (LCMS), with lower proportions of different bacteria strains (Brazelton et al., 2006; Schrenk et al., 2004). Three important metabolic reactions in the Lost City chimneys have been proposed: sulfate reduction,

methanogenesis and anaerobic methane oxidation (Brazelton et al., 2006; Kelley et al., 2005; Lang et al., 2018; Orcutt et al., 2011; Schrenk et al., 2004). Hydrothermal circulation is believed to be driven by residual crustal heat and lithospheric cooling, with the composition of the fluids controlled by subsurface serpentinization reactions in the underlying mantle rock. Based on radiocarbon dating, hydrothermal activity has been active for at least 30,000 yr (Früh-Green et al., 2003; Kelley et al., 2005), and subsequent U-Th analyses indicated that this is a minimum age as some of the carbonate deposits yielded ages of up to 120,000 yr (Ludwig et al., 2011).

2.1 IODP Expedition 357

IODP Expedition 357 drilled seventeen shallow boreholes (from 1.3 mbsf to maximum 16.4 mbsf) at nine sites along an east-west transect across the AM (Figure 1). Two sites are on the eastern end of the southern wall (Sites M0068 and M0075), three in the central section north of the LCHF (Sites M0069, M0072, and M0076), two on the western end (Sites M0071 and M0073), and two sites are to the north in the direction of the central dome and of IODP Site U1309 (Sites M0070 and M0074). The recovered mafic and ultramafic rocks reveal a high and heterogeneous degree of serpentinization and metasomatic talc-amphibole-chlorite overprinting and local rodingitization (Früh-Green et al., 2017, 2018). Contacts between ultramafic and gabbroic rocks are marked by silica metasomatism with talc, tremolite and chlorite (Holes M0068B, M0072B and M0076B) in part replacing pyroxenes. This indicates that hydration may have started at temperatures in the range of 400 - 500°C and that orthopyroxene alteration pre-dates the onset of serpentinization of olivine (Rouméjon, Früh-Green, et al., 2018; Schroeder & John, 2004). Field and geophysical studies estimate that at least ~20 % of the massif is completely serpentinized (Detrick & Collins, 1998; Früh-Green et al., 2003; Nooner et al., 2003). Two main stages of hydration can be distinguished: an initial stage of pervasive serpentinization at temperatures of 200 - 350°C (Boschi et al., 2008; Rouméjon, Früh-Green, et al., 2018; Rouméjon, Williams, et al., 2018) followed by a second stage dominated by focused fluid flow and leading to serpentine recrystallization and vein formation dominated by chrysotile or antigorite (Rouméjon, Früh-Green, et al., 2018).

This study focuses mainly on the five sites containing altered peridotite (Sites M0071, M0072, M0069, M0076 and M0068, Figure 2). The four remaining sites include foraminifera-bearing carbonate ooze, rubble blocks of variable lithologies and sedimentary breccia with volcanic clasts and carbonate sediments (Früh-Green et al., 2017). The studied sites had a core

recovery rate ranging between 30% (Hole M0071C) and 75% (Hole M0069A), with an average recovery rate of 58%. Drill cores of IODP Expedition 357 are described in detail in Früh-Green et al. (2017), Früh-Green et al (2018, supplementary material) and Rouméjon, Früh-Green, et al. (2018, supplementary material).

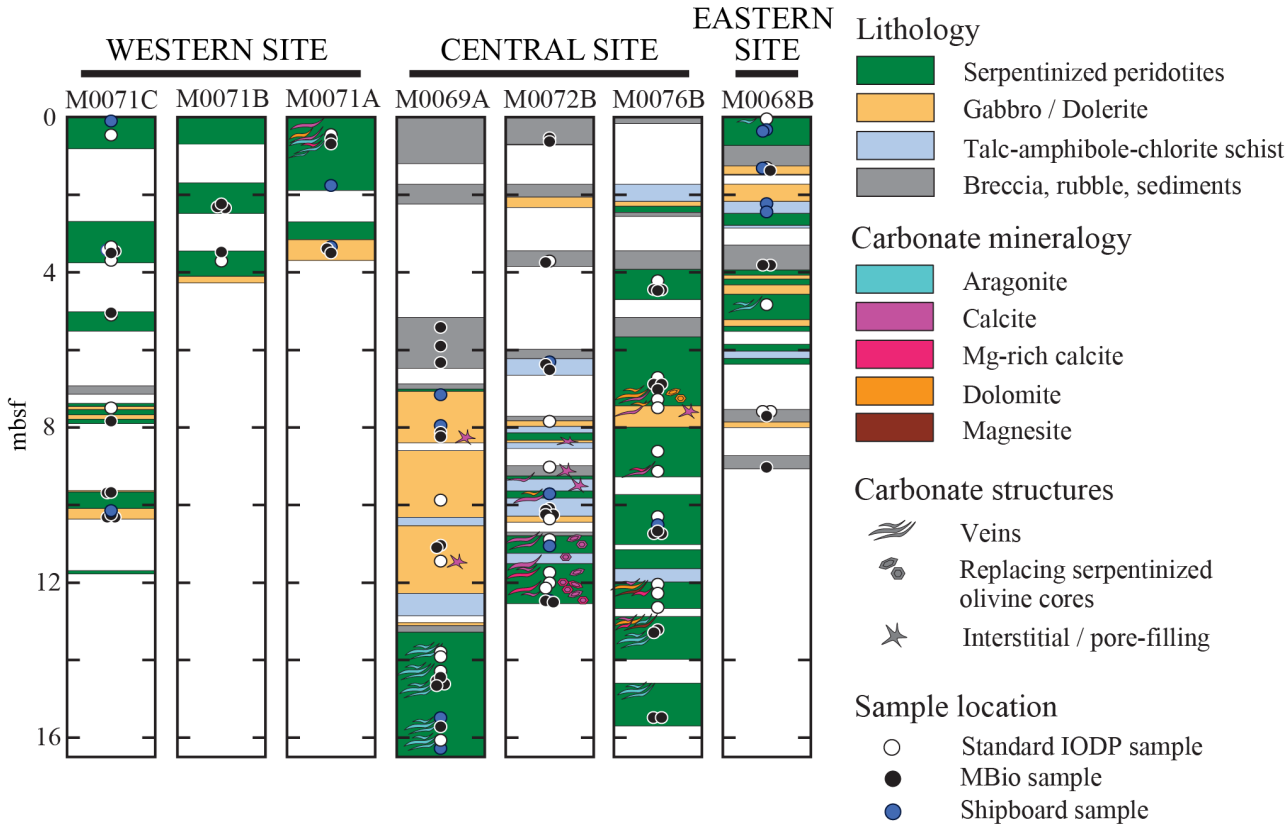

Figure 2. Simplified downhole logs (meters below seafloor = mbsf) of the dominant lithologies recovered in the seven Exp. 357 holes containing serpentinized peridotites. The western and eastern sites consist of rubbly intervals and sedimentary structures pointing to a mass-wasting origin and local faulting. The central sites represent *in-situ* portions of the detachment footwall (Früh-Green et al., 2017; Rouméjon et al., 2018a). Serpentinized peridotites from Hole M0071A, M0069A and M0068B are dominated by aragonite veins. In contrast, serpentinites from Hole M0072B have dominantly calcite and Mg-rich calcite in veins and serpentinized olivine cores, and one dolomite vein. Hole M0076B is the only hole that has aragonite, calcite, Mg-rich calcite, dolomite and magnesite veins, as well as dolomite in serpentinized olivine cores. The white dots indicate locations of standard IODP samples (sampled under non-sterile

conditions), the black dots are MBio samples and the blue dots are bulk rock shipboard samples analyzed during Exp. 357.

3 Analytical Methods

Isotopic investigations from eight sites (15 holes) of Expedition 357, covering the diversity of rock types and alteration textures, included 69 peridotites (42 harzburgites, 19 dunites and 8 serpentinite rubble samples), 33 mafic rocks (9 gabbroic rocks, 13 doleritic rocks) and 11 talc-amphibole ± chlorite schists. In addition, we measured clumped isotopes on 28 carbonate veins. Sample locations are shown in Figure 2, together with a simplified lithostratigraphy and location of identified carbonate features. Samples are named after IODP guidelines: Expedition_Drilling-Platform, Site, Hole_Core, Coretype_Section_Interval in cm; (e.g., 357_M0076B_9R_1_5-9). For simplicity, we have removed the expedition and drilling platform information that is the same for all samples (e.g., 76B_9R_1_5-9).

3.1 Sample Preparation

We determined concentrations of total carbon (TC), total inorganic carbon (TIC), and total non-carbonate carbon (TOC), and the isotopic compositions (δ^{13}C and δ^{18}O) of TIC, total carbon ($\delta^{13}C_{TC}$) and total non-carbonate carbon ($\delta^{13}C_{TOC}$). Sample preparation depended on whether the samples were collected under sterile conditions for microbiological studies (denoted as MBio samples) or whether the samples were obtained using standard IODP protocols (denoted as standard IODP samples). Onboard ship the MBio samples were immediately wrapped in acid-washed and autoclaved Teflon sheeting, frozen at -80°C in Whirl-Pak bags, and shipped frozen for further processing and subsampling at the Kochi Core Center Kochi University / JAMSTEC, Shikoku, Japan. There, the outsides of the frozen pieces of cores were carefully removed and subsampled while still frozen under clean air conditions and subsequently distributed for interlaboratory analyses. MBio_TIC denotes subsamples in which the internal material was crushed and homogenized using solvent-cleaned equipment, then wrapped in sterile Teflon sheeting and frozen at -20°C. Subsamples denoted as MBio_xTIC were rinsed 10 times in Milli-Q water before crushing and homogenization. A description of sample handling procedures during Expedition 357 can be found in Früh-Green et al. (2017). Because the MBio samples were already powdered or were pebbles collected from the cores, they could not be used for macro- or microscopic observations. Photographs of

the archive half and descriptions of the remaining cores made during the Expedition 357 sampling party provide a rough lithological and structural context for the MBio samples (Früh-Green et al., 2017; Früh-Green et al 2018, supplementary material).

The standard IODP samples are cut rock slabs or pebbles collected from the cores during the Exp. 357 onshore science party (Früh-Green et al., 2017). In our laboratory, the samples were cleaned by ultrasonication in 100 ml dichloromethane (DCM) for 5 min at room temperature and subsequently dried for 24 h at room temperature in a pre-combusted glass container covered with combusted aluminium foil. This cleaning step was not performed on the MBio powdered samples. The rocks slabs were then crushed, centrepieces collected and ground by hand using an agate mortar cleaned with DCM to obtain a homogenous powder. The TOC and $\delta^{13}C_{TOC}$ were determined on 200 mg aliquots, decarbonated with 3 ml of 3M hydrochloric acid (HCL). The remaining material was rinsed several times with Milli-Q water, dried at 70 °C overnight, and re-homogenized by hand using an agate mortar. For clumped isotope analyses and radiocarbon dating of carbonate veins, samples were cleaned with 2-propanol and compressed air. In the first step, the surfaces of the veins were removed and discarded, followed by sampling of the veins with a hand-held drill.

3.2 Powder X-ray Diffraction

Crystallographic analyses were made using a Bruker AXS D8 Advance Powder X-ray Diffractometer (XRD) equipped with a Lynxeye superspeed detector (Bruker Corporation, Billerica, United States) with Cu Kα radiation at a voltage of 45 kV and a current of 40 mA, with 2θ ranging between 10° to 60° with a step size of 0.01°, and measurement time of 1 s per step. Quantification of the mineralogy was carried out using the program PowDll (Kourkoumelis, 2013) and the RRUFF database (Lafuente et al., 2015).

3.3 Carbon Content and Isotopic Composition

TC and TOC contents and isotopic compositions were determined by combustion of 1 to 60 mg of sample using a FlashEA 1112 Elemental Analyzer (EA) interfaced via a Conflo IV to a Delta V Plus Isotope Ratio Mass Spectrometer (MS) (all ThermoFisher Scientific, Bremen, Germany). The carbon content was calculated using two standards (Bodenstandards No.5; 0.141 %TOC, HEKAtech, Wegberg, Germany, and nicotinamide; 59.01 %TOC, ThermoFisher Scientific, Milan, Italy). Empty tin capsules were measured for blank correction.

Analytical reproducibility of $\delta^{13}C_{TC}$ and $\delta^{13}C_{TOC}$ is ±0.11 ‰ (1σ). The detection limit for a reproducible carbon isotope measurement is about 1 µg C.

TIC contents were either measured on a CM 5012 CO_2 coulometer interfaced with a CM 5130 Acidification Module or were calculated by subtraction of TOC content from TC or by mass balance using Equation 1.

$$(f_{TC} * \delta^{13} C_{TC}) = (f_{TIC} * \delta^{13} C_{TIC}) + (f_{TOC} * \delta^{13} C_{TOC}) \quad \text{(Eq.1)}$$

For coulometric measurements, 20 to 30 mg of sample was weighed into glass capsules and reacted with 2M perchloric acid ($HClO_4$). Precision depended on the TIC content and was determined from internal laboratory standards and replicate analyses. Reproducibility for TIC is better than 2.5% for standards with more than 1 wt% carbon, and the maximum error for <600 ppm carbon is ± 30 ppm (see Schwarzenbach et al., 2013).

$\delta^{13}C$ and $\delta^{18}O$ of TIC were measured on a GasBench II connected to a Delta V mass spectrometer (both ThermoFisher Scientific, Bremen, Germany), as described in detail in Breitenbach & Bernasconi (2011). The average long term reproducibility based on replicate standards is ±0.10 ‰ for $\delta^{13}C$ and 0.11 ‰ for $\delta^{18}O$ (1 σ). The instrument was calibrated with the international standards NBS19 ($\delta^{13}C$ = 1.95 ‰ and $\delta^{18}O$ = -2.2 ‰) and NBS18 ($\delta^{13}C$ = -5.01 ‰ and $\delta^{13}O$ = -23.01 ‰). Samples as small as ~20 µg TIC can be analyzed with confidence and the precision mentioned above.

A subset of carbonate veins was analyzed for clumped isotopes (Δ47) on a Kiel IV carbonate device interfaced with a ThermoFisher Scientific MAT253 isotope ratio mass spectrometer following the methodology described in detail in Meckler et al. (2014) and Müller et al. (2017). Briefly, 100 to 110 µg of carbonate were reacted with three drops of 104 % phosphoric acid (H_3PO_4) at 70°C. The evolved CO_2 was purified on a custom-built Porapak Q trap held at -40°C and measured on a MAT253 in micro-volume mode using the long-integration dual-inlet (LIDI) Protocol (Hu et al., 2014; Müller et al., 2017). The results are converted to the Carbon Dioxide Equilibrium Scale (CDES) using the carbonate standards ETH-1, ETH-2 and ETH-3 as described in Bernasconi et al. (2018). Dolomite values are reported for a reaction temperature of 70°C, which is the same temperature used to establish the calibration (Müller et al., 2019), and calcites are projected to 25°C. With a reasonable amount of replicate analyses, the margins of error are ± 3 to 5°C for at the 95% CL (Fernández et al., 2017). However, due to the limited amount of available material, the number of replicate measurements was limited and varied between 1 and 10; thus, precision could not always be

reached. δ^{13}C and δ^{18}O of TIC and δ^{13}C of TC and TOC are reported in conventional delta notation (Equation 2) with respect to the Vienna Pee Dee Belemnite (VPDB) standard.

$$\left[\delta_x(‰) = \left(\frac{R_{sample}}{R_{standard}} - 1\right) * 1000\right] \quad \text{(Eq. 2)}$$

Clumped isotopes allow the calculation of δ^{18}O of the fluid in equilibrium with the carbonate vein. We used the calibration of Grossman & Ku (1986) for aragonite, O'Neil et al. (1969) corrected by Friedman & O'Neil (1977) for calcites and Müller et al. (2019) for dolomite precipitation. The error for the calculated δ^{18}O of the water depends on the number of replicate measurements.

3.4 Radiocarbon Ages

Radiocarbon ages of whole-rock and decarbonated samples were measured by combustion with an Elemental Analyzer interfaced to a MICADAS Accelerator Mass Spectrometer (AMS) (Synal et al., 2007) equipped with gas- ion source at the Laboratory of Ion Bean Physics, ETH Zurich, and detailed methods are reported in Ruff et al. (2010) and Wacker et al. (2010). Carbonate veins were measured by placing them in vacutainers which were purged for 10 minutes with He and converted to CO_2 through the addition of 85% H_3PO_4, followed by direct injection of the gas into the ion source of the AMS. The results are normalized against standard Oxalic Acid II (NIST SRM 4990C) and corrected with a radiocarbon blank CO_2 (IAEA C-1). In addition, IAEA-C2 and coral CSTD were measured in each run to test the accuracy of the measurement. The precision was better than ±5 ‰ on a modern standard. Radiocarbon data are expressed as $F^{14}C$ (fraction of modern carbon) and conventional ^{14}C ages, according to Reimer et al. (2004).

Table 1. Content and carbon and oxygen isotope compositions (VPDB) in total carbon (TC), total organic- (TOC), and total inorganic carbon (TIC), and carbonate formation temperature of gabbroic and ultramafic rocks from the southern wall at the Atlantis Massif.

Site	Hole	Core	Section	Interval (cm) top	Interval (cm) bot.	Depth (mbsf) top	Depth (mbsf) bot.	Type of the rock	MBio	TC (ppm)	TOC (ppm)	TIC (ppm)	$\delta^{13}C_{TC}$ (‰)	$\delta^{13}C_{TOC}$ (‰)	$\delta^{13}C_{TIC}$ (‰)	$\delta^{18}O_{TIC}$ (‰)	T^{a} (°C)
71	A	1	1	45	48	0.45	0.48	Serpentinized dunite		1407	384	1000*	-5.92	-25.88	2.18	4.38	-3
71	A	1	2	0	11	0.58	0.69	Serpentinized dunite	x	390634	1108	40630	0.71	-22.03	0.30	0.36	14
71	A	1	2	11	18	0.69	0.76	Serpentinized dunite	x	49044	315	49737*	0.95	-22.33	0.63	1.89	7
71	A	1	2	120	121	1.78	1.79	Serpentinized harzburgite		207			-20.55				
71	A	2	1	64	67	3.36	3.39	Metagabbro		203			-26.33				
71	A	2	1	67	77	3.39	3.49	Metagabbro	x	48	75		-17.66	-24.88			
71	A	2	1	77	86	3.49	3.58	Metagabbro	x	60	256		-25.33	-25.09			
71	B	2	1	53	58	2.25	2.30	Serpentinized rubble	x	119	251	63*	-13.57	-24.63	-3.64	-5.32	44
71	B	2	1	61	64	2.33	2.36	Serpentinized rubble	x	131	277		-12.83	-24.22			
71	B	2	1	64	66	2.36	2.38	Serpentinized rubble	x	93	265		-14.85	-24.50			
71	B	3	1	0	10	3.44	3.54	Serpentinized rubble	x	138	726	136*	-8.18	-23.10	-7.96	-11.15	85
71	B	3	1	27	29	3.71	3.73	Serpentinized rubble		152	220		-24.42	-25.26			
71	C	1	1	11	13	0.11	0.13	Serpentinized rubble		545	531*	14*	-24.98		-7.36	-9.76	74
71	C	1	1	46	50	0.46	0.50	Serpentinized harzburgite		262	318		-22.62	-25.47			
71	C	2	1	67	77	3.35	3.45	Serpentinized harzburgite		226	299		-21.79	-24.27			
71	C	2	1	74	76	3.42	3.44	Serpentinized harzburgite		309			-19.86				
71	C	2	1	78	84	3.46	3.52	Serpentinized harzburgite	x	130	225		-11.92	-23.38			
71	C	2	1	84	90	3.52	3.58	Serpentinized harzburgite	x	164	282		-7.43	-24.18			
71	C	2	CC	5	9	3.70	3.74	Serpentinized harzburgite		260	339		-19.93	-25.42			
71	C	3	1	0	10	5.02	5.12	Serpentinized harzburgite	x	180	268	185*	-8.09	-25.35	-8.59	-14.29	114
71	C	3	1	10	13	5.12	5.15	Serpentinized harzburgite		151	322		-20.98	-23.86			
71	C	5	1	20	23	7.58	7.61	Serpentinized harzburgite		295	373		-21.40	-24.17			
71	C	5	CC	5	10	7.84	7.89	Serpentinized harzburgite	x	145	363		-10.68	-25.41			
71	C	6	1	55	57	10.18	10.20	Dolerite rubble		801	679*	122*	-22.82		-8.15	-13.08	102
71	C	6	1	64	70	10.27	10.33	Dolerite rubble	x	177	251		-12.45	-25.93			
71	C	6	1	70	74	10.33	10.37	Dolerite rubble	x	213	252		-10.37	-25.54			
71	C	6	1	70	74	10.33	10.37	Dolerite rubble	x	224	162		-14.84	-25.93			
71	C	9	1	0	7	9.67	9.74	Serpentinized rubble	x	189	336		-10.46	-25.00			
71	C	9	1	10	14	9.77	9.81	Serpentinized rubble	x	80	229		-14.24	-24.38			
69	A	5	1	30	32	7.18	7.20	Metadolerite		445			-24.69				
69	A	5	1	110	115	7.98	8.03	Metadolerite		299			-25.48				
69	A	5	1	129	145	8.17	8.33	Metadolerite	x	60	233	44*	-13.13	-27.34	-8.10	-10.64	81
69	A	5	1	137	151	8.25	8.39	Metadolerite	x	75	220		-20.29	-25.52			
69	A	5	1	137	151	8.25	8.39	Metadolerite	x		154			-26.88			
69	A	6	1	127	130	9.87	9.90	Metadolerite		186	234		-25.44	-27.04			
69	A	7	1	73	75	11.05	11.07	Metadolerite	x	78	200		-18.51	-23.29			
69	A	7	1	80	82	11.12	11.14	Metadolerite	x	78	51*	28*	-20.88		-12.48	-15.20	124
69	A	8	1	14	18	11.46	11.50	Metadolerite		95	211	35*	-21.32	-26.63	-12.35	-14.76	119
69	A	9	2	43	44	13.80	13.81	Serpentinized harzburgite		23304			0.52		0.20	2.51	5
69	A	9	2	57	61	13.94	13.98	Serpentinized harzburgite		169	179	179	-17.99	-25.85	-2.77	-4.33	37
69	A	9	2	91	93	14.28	14.30	Serpentinized harzburgite		531	213	213	-1.62	-23.63	0.59	1.43	9
69	A	9	2	106	114	14.43	14.51	Serpentinized dunite	x	7564	466	466	1.37	-24.51	1.46	3.75	-1
69	A	9	2	118	124	14.55	14.61	Serpentinized dunite	x	5822	133	133	1.10	-26.71	0.78	1.91	7
69	A	9	2	124	129	14.61	14.66	Serpentinized dunite	x	5123	135	135	0.54	-26.96	0.91	1.42	9
69	A	9	2	129	133	14.66	14.70	Serpentinized dunite	x	5927			0.70		0.02	0.30	14
69	A	10	1	80	87	15.52	15.59	Serpentinized harzburgite		3631	39*	39*	-0.71	-25.45	-0.44	1.52	9
69	A	10	1	104	124	15.76	15.96	Serpentinized harzburgite	x	6560	141	141	0.76	-27.73	0.60	3.07	2
69	A	10	2	14	16	16.08	16.10	Serpentinized harzburgite		12578	255	255	-0.22	-24.12	1.63	4.74	-5
69	A	10	3	0	25	16.29	16.54	Serpentinized dunite		1204	-60*	-60*	-10.87		-11.56	-14.38	115

continued on next page

Table 1. (continued)

Site	Hole	Core	Section	Interval (cm) top	Interval (cm) bot.	Depth (mbsf) top	Depth (mbsf) bot.	Type of the rock	MBio	TC (ppm)	TOC (ppm)	TIC (ppm)	$\delta^{13}C_{TC}$ (‰)	$\delta^{13}C_{TOC}$ (‰)	$\delta^{13}C_{TIC}$ (‰)	$\delta^{18}O_{TIC}$ (‰)	T[a] (°C)
72	B	5	1	37	38	6.36	6.37	Talc/amphi./chlorite schist		272			-24.93				
72	B	5	1	40	43	6.39	6.42	Talc/amphi./chlorite schist	x	139	503*	106	-9.67	-20.32	-6.36	-9.90	75
72	B	5	1	53	56	6.52	6.55	Talc/amphi./chlorite schist	x	171	103		-16.14	-23.23			
72	B	6	1	15	18	7.86	7.89	Rodingitized gabbro		174	114		-22.50	-25.35			
72	B	7	1	55	58	9.54	9.57	Talc/amphi./chlorite schist			114			-23.57			
72	B	7	1	73	75	9.71	9.74	Serpentinized harzburgite		566	193*	374*	-11.62		-4.49	-16.21	136
72	B	7	1	109	115	10.08	10.14	Talc/amphi./chlorite schist	x	165	107		-22.70	-26.58			
72	B	7	1	115	125	10.14	10.24	Talc/amphi./chlorite schist	x	65	46		-16.07	-24.07			
72	B	7	1	126	136	10.25	10.35	Talc/amphi./chlorite schist	x	148	99		-26.22	-25.31			
72	B	7	1	126	136	10.25	10.35	Talc/amphi./chlorite schist	x	75			-23.66				
72	B	7	CC	9	13	10.38	10.42	Rodingitized gabbro		117	183		-24.43	-26.39			
72	B	8	1	19	22	10.90	10.93	Serpentinized harzburgite		439	359		-9.39	-24.35			
72	B	8	1	34	38	11.05	11.09	Serpentinized harzburgite		1308	781*	527*	-17.71		-6.23	-14.87	120
72	B	8	2	26	30	11.77	11.81	Serpentinized harzburgite		2152	710*	2009	-4.18	-26.61	-2.57	-19.83	191
72	B	8	2	50	51	12.00	12.02	Serpentinized harzburgite		397	512		-9.05	-24.88			
72	B	8	2	67	70	12.18	12.20	Serpentinized harzburgite		251	679		-13.89	-26.17			
72	B	8	2	76	77	12.27	12.28	Serpentinized harzburgite		1372	330*	1042*	-8.00		-2.47	-11.48	88
72	B	8	CC	0	5	12.28	12.33	Serpentinized harzburgite	x	759	662*	650	-11.91	-27.98	-9.22	-12.52	97
72	B	8	CC	5	20	12.33	12.48	Serpentinized harzburgite	x	532	135	1020	-5.65	-27.50	-5.68	-16.47	140
76	B	3	1	78	83	4.22	4.27	Serpentinized dunite		256	290		-15.16	-25.74			
76	B	3	1	100	125	4.44	4.69	Serpentinized dunite	x	1180	303*	1111	0.72	-19.83	1.99	1.08	11
76	B	3	1	100	125	4.44	4.69	Serpentinized dunite	x	655	177*	598	-0.62	-21.94	1.42	1.03	11
76	B	3	1	102	110	4.46	4.54	Serpentinized dunite	x	858	237*	802	0.41	-23.52	2.07	3.15	2
76	B	4	2	28	31	6.74	6.77	Serpentinized harzburgite		246	365*	31	-24.31	-27.56	-1.60		
76	B	5	1	14	28	6.87	7.01	Serpentinized dunite	x	398	234*	358	-7.65	-27.28	-5.49	-13.48	106
76	B	5	1	14	28	6.87	7.01	Serpentinized dunite	x	651	279*	580	-1.86	-25.63	1.04	-1.83	24
76	B	5	1	28	36	7.01	7.09	Serpentinized dunite	x	1384	288	1080	0.34	-27.98	1.57	-4.41	38
76	B	5	1	55	59	7.28	7.32	Serpentinized dunite		8092	266*	7808	1.43	-25.78	2.42	4.26	-3
76	B	5	1	77	80	7.50	7.53	Metagabbro		168	144		-18.13	-25.76			
76	B	6	1	63	65	8.61	8.63	Serpentinized harzburgite		235	201		-16.90	-25.27			
76	B	6	1	118	122	9.16	9.20	Serpentinized harzburgite		356	282		-18.47	-25.55			
76	B	7	1	60	62	10.32	10.34	Serpentinized harzburgite		273	221		-19.54	-25.49			
76	B	7	1	81	83	10.53	10.55	Serpentinized harzburgite		2283	146*	2137*	0.06	-25.45	1.81	1.73	8
76	B	7	1	95	105	10.67	10.77	Serpentinized harzburgite	x	217	235		-10.14	-25.51			
76	B	7	1	105	120	10.77	10.92	Serpentinized harzburgite	x	234	179*	157	-12.06	-25.80	-5.34	-10.55	80
76	B	7	1	105	120	10.77	10.92	Serpentinized harzburgite	x	509	253*	462	-2.24	-25.51	0.12	-2.37	27
76	B	8	1	90	94	12.05	12.09	Serpentinized harzburgite		320	288		-21.46	-25.92			
76	B	8	1	112	117	12.27	12.32	Serpentinized harzburgite		26599	1665*	10254	-2.34	-3.66	-0.24	-6.42	51
76	B	8	1	148	151	12.63	12.66	Serpentinized harzburgite		262	266		-23.46	-26.72			
76	B	9	1	34	41	13.21	13.28	Serpentinized harzburgite	x	10414	164	10860	0.60	-28.31	0.31	4.75	-5
76	B	9	1	43	52	13.30	13.39	Serpentinized harzburgite	x	101	151*	49	-16.67	-25.25	-7.72	-6.73	53
76	B	10	1	91	111	15.50	15.70	Serpentinized dunite	x	136	120*	45	-21.31	-27.90	-7.90	-7.93	61
76	B	10	1	91	111	15.50	15.70	Serpentinized dunite	x	1567	147	1540	1.14	-28.00	1.68	0.86	12
68	A	1	1	12	21	0.12	0.21	Talc/amphi. schist	x	63	213		-13.36	-24.29			
68	B	1	1	10	13	0.10	0.13	Serpentinized harzburgite		85	158		-24.69	-25.57			
68	B	1	1	34	35	0.34	0.35	Serpentinized harzburgite		219			-25.27				
68	B	1	1	38	40	0.38	0.40	Serpentinized harzburgite		531	483*	48	-23.88		-8.21	-13.85	110
68	B	1	1	132	135	1.32	1.35	Metagabbro		72	161*	38*	-15.41	-25.07	-6.92	-11.77	90
68	B	1	1	134	139	1.34	1.39	Metagabbro		210			-15.92				
68	B	1	1	139	144	1.39	1.44	Metagabbro	x	708	168*	662	0.58	-23.98	2.27	3.85	-1
68	B	2	1	31	36	2.03	2.08	Talc/amphi./chlorite schist		493			-22.50				
68	B	2	1	52	55	2.24	2.27	Talc/amphi./chlorite schist		187			-25.65				
68	B	4	1	84	87	4.84	4.87	Serpentinized dunite		439	496*	186	-18.74	-26.22	-8.57	-16.17	136

* Calculated carbon content using equation; [a] Calculated oxygen isotope temperatures

4 Results

Five sites with altered peridotites (Sites M0071, M0072, M0069, M0076 and M0068) make up the focus of this study and can be divided into two groups. The northwestern (M0071) and most eastern sites (M0068) contain varying proportions of ultramafic, mafic and sedimentary rocks that have been interpreted as originating from mass-wasting and local faulting processes (Früh-Green et al., 2017; Rouméjon, Früh-Green, et al., 2018). These holes can be used to interpret the general alteration history of the Atlantis Massif but should be considered with caution for more detailed and depth-dependent interpretations. The sites from the central part of the southern wall (M0072, M0069, M0076) are considered *in-situ* portions of the Atlantis Massif indicated by coherent, decimeter- to meter-long sections of cores, as well as consistent structural measurements (Früh-Green et al., 2017, 2018).

Veins are the most abundant carbonate occurrence in the Atlantis Massif basement and tend to be concentrated in the serpentinites from the central drill sites closest to the LCHF (M0069, M0072, M0076) (Figure 2). The veins are composed of calcite, dolomite, magnesite and aragonite in variable proportions. Magnesite veins are the least frequent, occurring exclusively in association with dolomite and limited to the deeper sections of Hole M0076B (> 12 mbsf). The most abundant and volumetrically dominant vein type are up to 1 cm wide aragonite veins that are observed throughout the ultramafic rocks at Hole M0069A, in the deeper section of Hole M0076B (> 13 mbsf), in the top cores from Holes M0071A and M0068B, and on the altered surface of a deeper sample from Hole M0068B (Figure 2). The aragonite veins crosscut the primary rock fabric and postdate all secondary fabrics, indicating that they are the last to be formed.

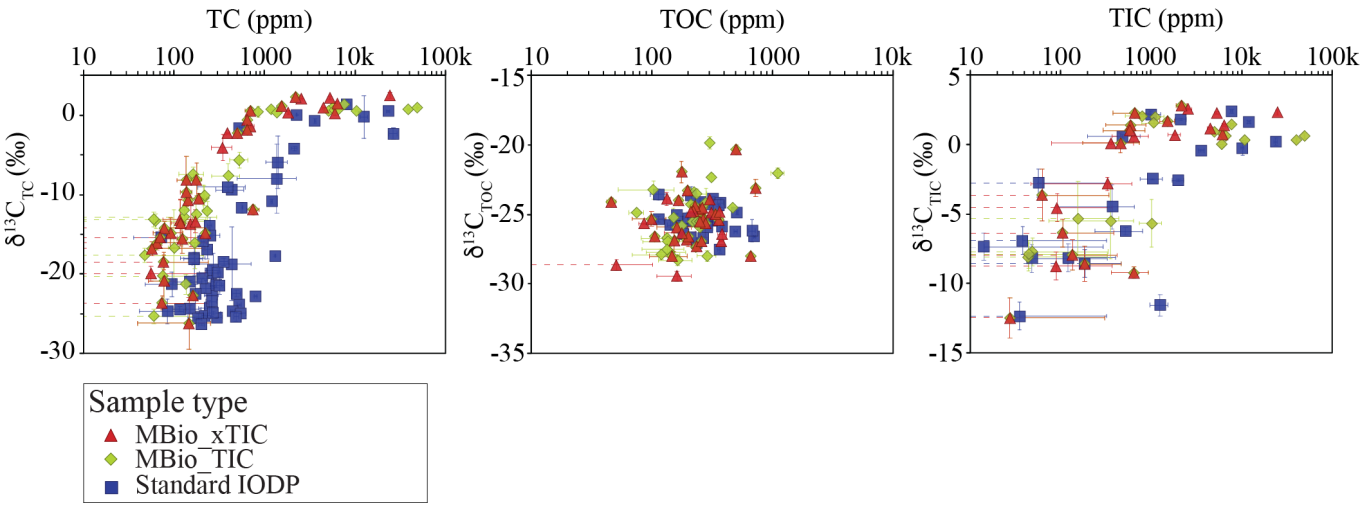

Figure 3. (a) Variations in total carbon content (TC) vs $\delta^{13}C_{TC}$, (b) total organic carbon content (TOC) vs $\delta^{13}C_{TOC}$, and (c) total inorganic carbon content (TIC) vs $\delta^{13}C_{TIC}$. See text for the distinction between standard IODP samples, MBio_TIC and MBio_xTIC samples. The dotted lines represent error bars continuing outside the figure scale.

4.1 Carbon Geochemistry

Comparing results from the sterile MBio rocks samples (rinsed and non-rinsed) with samples collected with regular IODP sampling protocol offers the possibility to evaluate possible procedural contaminations (Figure 3). Considering the natural heterogeneities of the rocks, samples with TC > 0.1 wt% show similar concentrations and isotopic compositions, independent of the handling procedure. Samples with TC < 0.1 wt% show minor variations, whereby the MBio sample sets show no difference between each other but tend to have less TC than the standard IODP samples but still within the range of error. No noticeable differences are seen in TIC and TOC contents and isotopic compositions related to handling protocols.

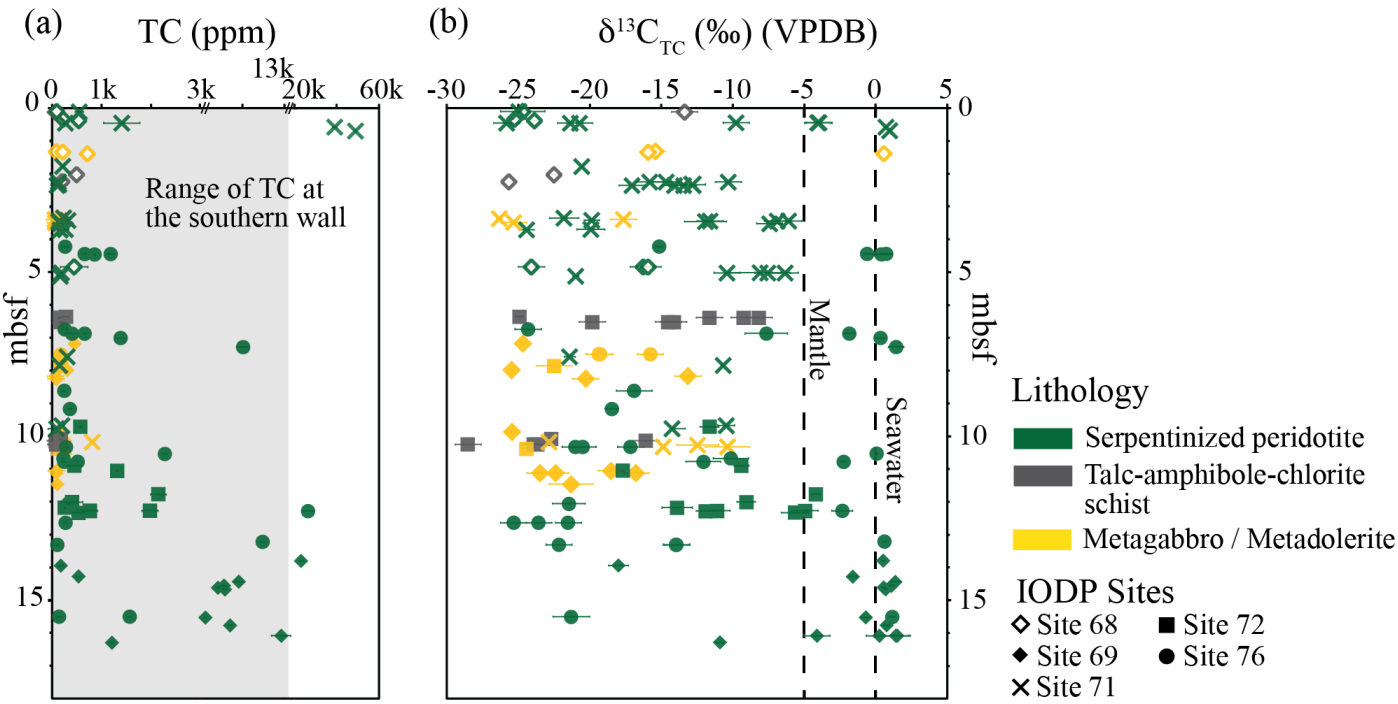

Figure 4. (a) Variations in total carbon (TC) content and (b) $\delta^{13}C_{TC}$ values with depth below seafloor (mbsf) in serpentinized peridotites, gabbroic rocks and metasomatic fault rocks from

the southern wall at the AM. Average isotopic composition of mantle and seawater carbon are shown as dashed lines. Grey shaded region marks the range of TC content at the southern wall from the previous study of Delacour et al. (2008).

4.1.1 Basement Rocks

Carbon contents and isotope compositions are given in Table 1. The basement rocks show a wide range of TC varying from 48 ppm to 5 wt% and $\delta^{13}C_{TC}$ values from -26.3 to +1.4 ‰. The majority of the samples have less than 0.2 wt% TC (see Figure 4). Gabbroic rocks and talc-amphibole chlorite schists have less variable TC contents with an average concentration below 202 ppm and a maximum of 801 ppm. The TC in serpentinites range from 80 ppm to 4.9 wt%; with the higher concentrations observed in the upper 0.7 mbsf at Hole M0071A, in the deeper parts of Holes M0069A and M0072B and throughout Hole M0076B. Variations in $\delta^{13}C_{TC}$ mainly reflect variations in carbonate contents. The majority of the mafic rocks have TIC contents below 123 ppm and $\delta^{13}C_{TIC}$ values from -12.5 to -6.4 ‰ (Figure 5a, 5c). The serpentinites show TIC content ranging from below detection limit to 5.0 wt% with $\delta^{13}C_{TIC}$ ranging between -11.6 and +2.4 ‰. Most serpentinites with TIC above 500 ppm have $\delta^{13}C_{TIC}$ values around -0.6 ‰, which is in the range of marine carbonates (e.g., Zeebe & Wolf-Gladrow, 2001). The serpentinites with lower TIC content generally have more negative $\delta^{13}C_{TIC}$ ranging between -8.6 and +0.6 ‰. Six serpentinites with TIC > 500 ppm also have negative $\delta^{13}C_{TIC}$ values between -11.6 ‰ and -2.5 ‰. These samples are all, except one, from Hole M0072B. TOC concentrations range from below detection limit to 0.1 wt%, and the $\delta^{13}C$ from -28.3 to -19.8 ‰ (see Figure 5b, 5d). TOC contents are generally below 260 ppm in the mafic rocks and average 309 ppm in the serpentinites, with many higher than 500 ppm. Higher TOC concentrations are observed in the upper meters of the cores and more frequently at Hole M0072B.

4.1.2 Carbonate Veins

The $\delta^{13}C$ of the veins lie in a narrow range from -3.0 to +2.3 ‰, typical for marine carbonates (Figure 6, Table 2). Dolomites have slightly more ^{13}C-depleted values of -2.7 to + 0.2 ‰ (n = 5). The calcites (n = 16) show a distinction between Holes M0072B and M0076B, with an average $\delta^{13}C$ of -1.2 ‰ and +2.0 ‰, respectively. $\delta^{13}C$ of the aragonite veins range

from -1.5 to +1.6 ‰ (n = 7) and show a distinction between Hole M0076B with slightly more depleted values (-1.5 to -0.1 ‰) and Hole M0069A (-0.2 to +1.6 ‰).

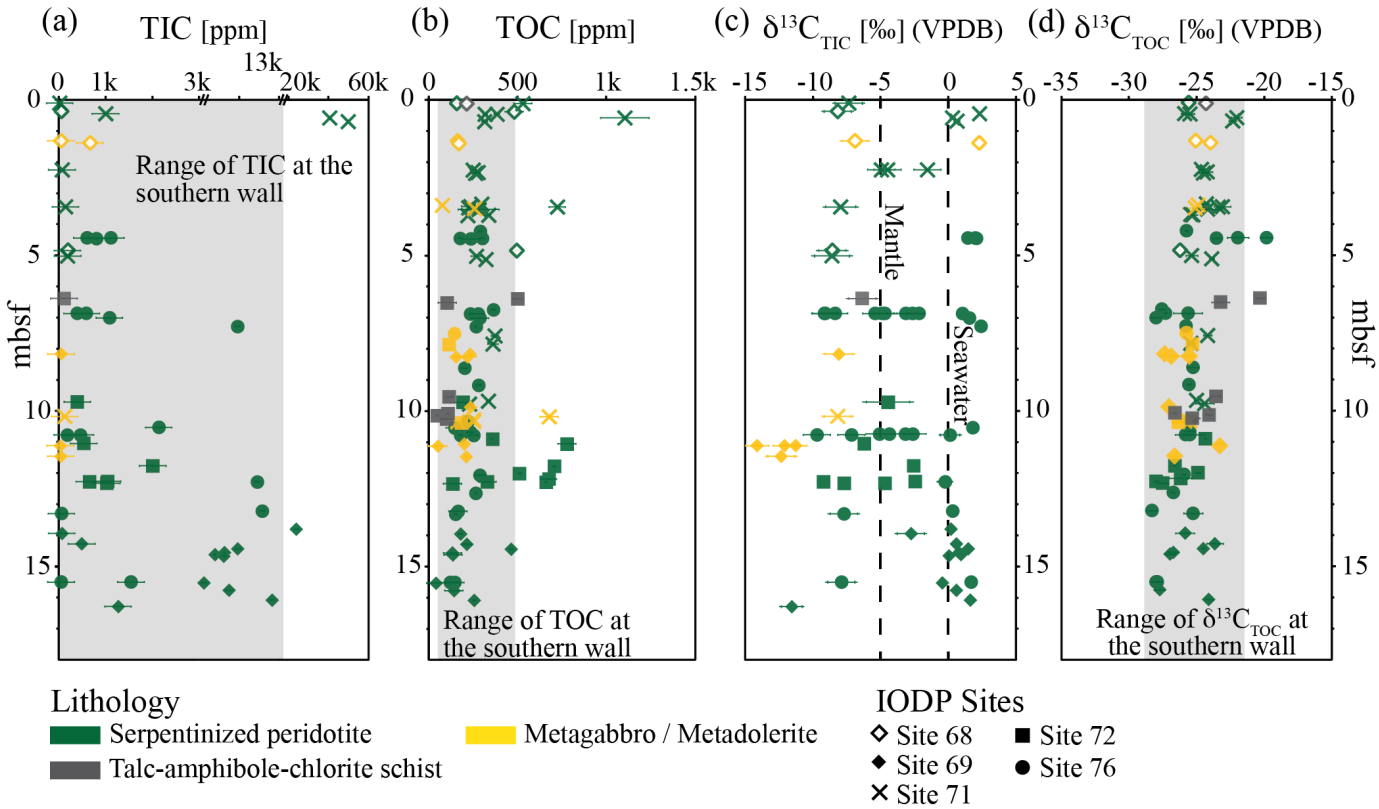

Figure 5. (a) Variations in total inorganic carbon (TIC) content, (b) total organic carbon (TOC) content, (c) $\delta^{13}C_{TIC}$ values and (d) $\delta^{13}C_{TOC}$ values with depth below seafloor in serpentinized peridotites, gabbroic rocks and metasomatic fault rocks at the southern wall at the Atlantis Massif. Average isotopic composition of mantle - and seawater carbon are shown as dashed lines. Grey shaded region marks the range of TIC -, TOC content and isotopic composition at the southern wall from the previous study of Delacour et al. (2008).

4.2 Oxygen Isotopes

4.2.1 Bulk rock Carbonate

The overall inorganic carbon concentration of the mafic rocks is very low; thus, only seven samples could be measured. They have low $\delta^{18}O_{TIC}$ values of -15.2 to -9.9 ‰ (VPDB) except for one sample located below a highly brecciated area with a $\delta^{18}O_{TIC}$ = +3.9 ‰. This is interpreted to be related to late precipitation from seawater (Figure 7a). The ultramafic rocks

exhibit a wide range of $\delta^{18}O_{TIC}$ values from -19.8 to +4.7 ‰. No downhole trend in $\delta^{18}O_{TIC}$ can be observed; however, some general patterns are visible across the different sites. The $\delta^{18}O_{TIC}$ from ultramafic rocks from Hole M0071A and Site M0069 show relatively high $\delta^{18}O_{TIC}$ ranging between -4.3 and +4.7 ‰ except one sample with $\delta^{18}O_{TIC}$ of -14.4‰. Sites M0072, M0068 and Hole M0071B and M0071C are characterized by overall ^{18}O- depleted values between -19.8 and -5.3 ‰, whereas Site M0076, closest to the LCHF, shows $\delta^{18}O_{TIC}$ values varying from -13.5 to +4.8 ‰.

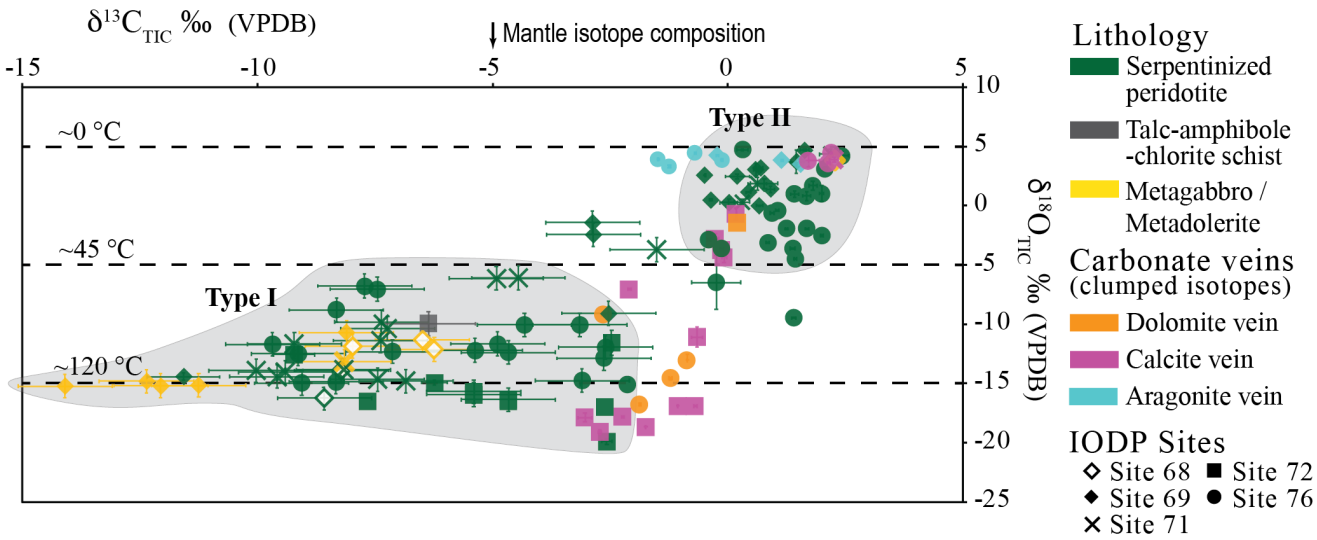

Figure 6. Variations in $\delta^{13}C$ versus $\delta^{18}O$ of carbonates in serpentinized peridotites, gabbroic rocks and metasomatic fault rocks from the southern wall at the Atlantis Massif. Whole-rock samples are compared with clumped isotope results of calcite, aragonite and dolomite veins from four different holes. Distinction between Type I and Type II carbonates is marked as grey ellipses. Calculated temperatures using oxygen isotopes are shown as dashed lines.

4.2.2 Carbonate Veins

The $\delta^{18}O$ of the veins vary over a range of -19.1 to +4.4 ‰ (Figures 6 and 7a). Dolomites vary from -16.8 to -9.2 ‰, with one outlier around -1.4 ‰. The calcite veins from Hole M0072B have the most ^{18}O- depleted values from -19.1 to -0.7 ‰ with a decreasing trend with increasing depth. These ^{18}O-depleted values are distinct from the calcite veins in Holes M0076B and M0071A, which show compositions ranging from +3.6 to +4.4 ‰. Aragonite

veins have uniform $\delta^{18}O$ values from +3.3 to +4.4 ‰, similar to the calcite veins from Hole M0076B and M0071A.

4.3 Carbonate Precipitation Temperatures

4.3.1. Oxygen Isotope Temperatures of bulk rock TIC

Figure 7b shows estimated temperatures calculated from the bulk rock oxygen isotope data, using the fractionation equation for calcite-water of O'Neil et al. (1969) corrected in Friedman & O'Neil (1977) and assuming that all carbonate is calcite. For $\delta^{18}O_{Fluid}$, we used the end-member LCHF vent fluid composition of 0.4 ‰ (VSMOW) (Kelley et al., 2005). The calculated carbonate formation temperatures range from ambient to 191°C, with carbonates from Hole M0072B showing the highest temperatures. Carbonates from the mafic rocks formed exclusively at higher temperatures between 75 to 124°C, with one exception giving ambient temperatures. The ultramafic rocks exhibit a wide range of temperatures but show no downhole trends; however, some general patterns are apparent across the different sites. Carbonates from Hole M0071A and Site M0069 formed at temperatures < 39°C, except for the deepest serpentinite of Hole M0069A that yielded a temperature of > 100°C. Carbonates from Sites M0072 and M0068 and Holes M0071B and M0071C are characterized by precipitation temperatures of 44 to 191°C, with Site M0072 showing the highest temperatures consistently > 88°C. Site M0076 shows a wide range of temperatures varying from ambient to 106°C.

Two samples from different sites and depths have calculated precipitation temperatures slightly below 0°C, inconsistent with minimum seawater temperatures in the area. However, negative temperatures have been reported previously in peridotite-hosted carbonate veins (e.g., Bonatti et al., 1980; Eickmann et al., 2009; Früh-Green et al., 2003). ^{18}O-enriched compositions in carbonates can be caused by isotopic disequilibrium between HCO_3^- and $CO_{2(aq)}$ within the hydrothermal fluid due to kinetic fractionation between the bicarbonate and $CO_{2(aq)}$, for example, under conditions of rapid CO_2 loss (Hendy, 1971). Another explanation is that the carbonates formed during a glacial maximum when the $\delta^{18}O$ of the North-Atlantic deep-sea water was ~1.2 ‰ higher than present-day (Schrag et al., 2002). Another possibility is that rock-dominated fluid-rock interaction produced fluids with higher $\delta^{18}O$ values than assumed. For example, calculated temperatures would be higher by 5 to 10°C if a $\delta^{18}O_{Fluid}$ of +2 ‰ is used.

Table 2. Clumped isotope composition of carbonate veins and calculated $\delta^{18}O$ of the fluid in ultramafic rocks from the southern wall at the Atlantis Massif.

Site	Hole	Core	Section	Interval (cm)		Depth (mbsf)		Type of the rock	Mineral	#	$\delta^{13}C$ (VPDB)		$\delta^{18}O$ (VPDB)		Δ47		Temperature		$\delta^{18}O_{Fluid}$ (SMOW)[a]
				top	bot.	top	bot.				(‰)	σ	(‰)	σ	(‰)	σ	(°C)	68% CL	(‰)
71	A	1	1	24	28	0.24	0.28	Serpentinized dunite	Calcite	11	2.26	0.09	3.90	0.19	0.690	0.073	22	7	5.35
69	A	9	2	57	61	13.94	13.98	Serpentinized harzburgite	Aragonite	9	-0.22	0.03	4.23	0.04	0.771	0.069	1	5	0.51
69	A	10	1	15	18	14.87	14.90	Serpentinized harzburgite	Aragonite	10	1.56	0.03	3.51	0.05	0.750	0.038	5	3	0.77
69	A	10	1	104	124	15.76	15.96	Serpentinized harzburgite	Aragonite	9	1.16	0.02	3.83	0.02	0.740	0.030	7	3	1.58
72	B	7	1	28	30	9.27	9.29	Serpentinized dunite	Calcite	3	0.18	0.00	-0.71	0.52	0.613	0.045	45	12	
72	B	7	1	28	30	9.27	9.29	Serpentinized dunite	Calcite	9	-0.08	0.05	-4.35	0.47	0.623	0.049	42	7	0.99
72	B	7	1	28	30	9.27	9.29	Serpentinized dunite	Calcite	2	-0.65	0.12	-11.11	0.86	0.569	0.022	62	12	
72	B	7	1	75	77	9.74	9.76	Serpentinized harzburgite	Calcite	8	-0.14	0.01	-3.78	0.04	0.654	0.046	32	6	-0.39
72	B	7	1	75	77	9.74	9.76	Serpentinized harzburgite	Dolomite	10	0.22	0.05	-1.44	0.13	0.605	0.032	33	4	-0.54
72	B	7	1	75	77	9.74	9.76	Serpentinized harzburgite	Calcite	3	-2.09	0.04	-7.05	0.05	0.643	0.011	34	3	
72	B	8	1	19	22	10.90	10.93	Serpentinized harzburgite	Calcite	5	-0.26	0.08	-2.77	0.38	0.658	0.025	30	4	0.23
72	B	8	1	19	22	10.90	10.93	Serpentinized harzburgite	Calcite	10	-3.03	0.15	-17.90	0.37	0.430	0.055	146	14	-0.51
72	B	8	1	69	69	11.40	11.43	Serp. harz. and talc/amphi. schist	Calcite	1	-1.06	-	-16.91	-	0.425	-	144	-	
72	B	8	1	69	69	11.40	11.43	Serp. harz. and talc/amphi. schist	Calcite	8	-0.69	0.04	-16.92	0.05	0.427	0.030	144	9	0.34
72	B	8	1	26	30	11.77	11.81	Serpentinized harzburgite	Calcite	8	-2.72	0.04	-19.12	0.20	0.383	0.019	184	8	0.74
72	B	8	1	67	70	12.18	12.20	Serpentinized harzburgite	Calcite	1	-1.74	-	-18.67	-	0.424	-	145	-	
72	B	8	1	67	70	12.18	12.20	Serpentinized harzburgite	Calcite	2	-2.23	0.02	-17.84	0.09	0.421	0.024	149	25	
76	B	5	1	48	50	7.21	7.23	Serpentinized dunite	Dolomite	9	-1.87	0.01	-16.78	0.08	0.352	0.026	188	10	1.83
76	B	5	1	48	50	7.21	7.23	Serpentinized dunite	Calcite	11	2.14	0.03	3.59	0.08	0.737	0.034	8	3	1.71
76	B	5	1	55	59	7.28	7.32	Serpentinized dunite	Calcite	3	1.72	0.23	3.82	0.52	0.783	0.023	-3	3	
76	B	5	1	55	59	7.28	7.32	Serpentinized dunite	Calcite	14	2.20	0.02	4.44	0.04	0.741	0.027	7	2	2.30
76	B	8	1	112	117	12.27	12.32	Serpentinized harzburgite	Dolomite	9	-1.21	0.03	-14.56	0.13	0.386	0.035	154	11	1.78
76	B	8	1	112	117	12.27	12.32	Serpentinized harzburgite	Dolomite	1	-0.86	-	-13.04	-	0.511	-	70	-	
76	B	9	1	5	9	12.92	12.96	Serpentinized harzburgite	Aragonite	9	-0.12	0.02	3.85	0.05	0.764	0.028	1	2	0.28
76	B	9	1	5	9	12.92	12.96	Serpentinized harzburgite	Aragonite	10	-0.69	0.02	4.43	0.07	0.777	0.038	-2	3	0.19
76	B	9	1	5	9	12.92	12.96	Serpentinized harzburgite	Dolomite	13	-2.65	0.03	-9.21	0.10	0.493	0.046	82	8	-0.22
76	B	9	1	70	73	13.57	13.60	Serpentinized harzburgite	Aragonite	10	-1.47	0.01	3.93	0.04	0.761	0.033	2	3	0.54
76	B	10	1	8	11	14.67	14.70	Serpentinized harzburgite	Aragonite	10	-1.24	0.01	3.31	0.09	0.754	0.023	4	2	0.28

[a] Calculated oxygen isotope composition of the fluids

4.3.2 Clumped Isotope Temperatures of Carbonate Veins

Clumped isotope temperatures of the carbonate veins vary from ambient to 188°C, a range similar to that calculated from the $\delta^{18}O$ of bulk rock samples (Table 2). The calcite veins show the highest variability of formation temperatures, from ambient to 184°C, whereas dolomite veins yield formation temperatures between 70 and 188°C, except for one outlier at 33°C. The consistency of the clumped isotope temperatures with those estimated from ^{18}O suggests that the maximum temperatures of precipitations are preserved, and the carbonates have not undergone bond reordering upon cooling. Within this range, clear distinctions can be identified. The calcite veins from Hole M0072B show the highest temperatures with a distinct separation between moderate temperatures ($T_{\Delta 47}$ = 40) in the upper section and high temperatures ($T_{\Delta 47}$ = 152°C) below 11 mbsf (Figure 7b). The higher temperatures distinctly separate calcite veins in Hole M0072B from the calcite veins in Holes M0076B and M0071A, which formed at low temperatures with $T_{\Delta 47}$ < 22 °C. Aragonite veins show temperatures of less than 7°C, similar to calcite veins from Hole M0076B and M0071A. One calcite vein and one aragonite vein show $\Delta 47$ – temperatures slightly below 0°C, indicating disequilibrium precipitation. Possible mechanisms causing high $\Delta 47$ are discussed in detail in section 4.3.1.

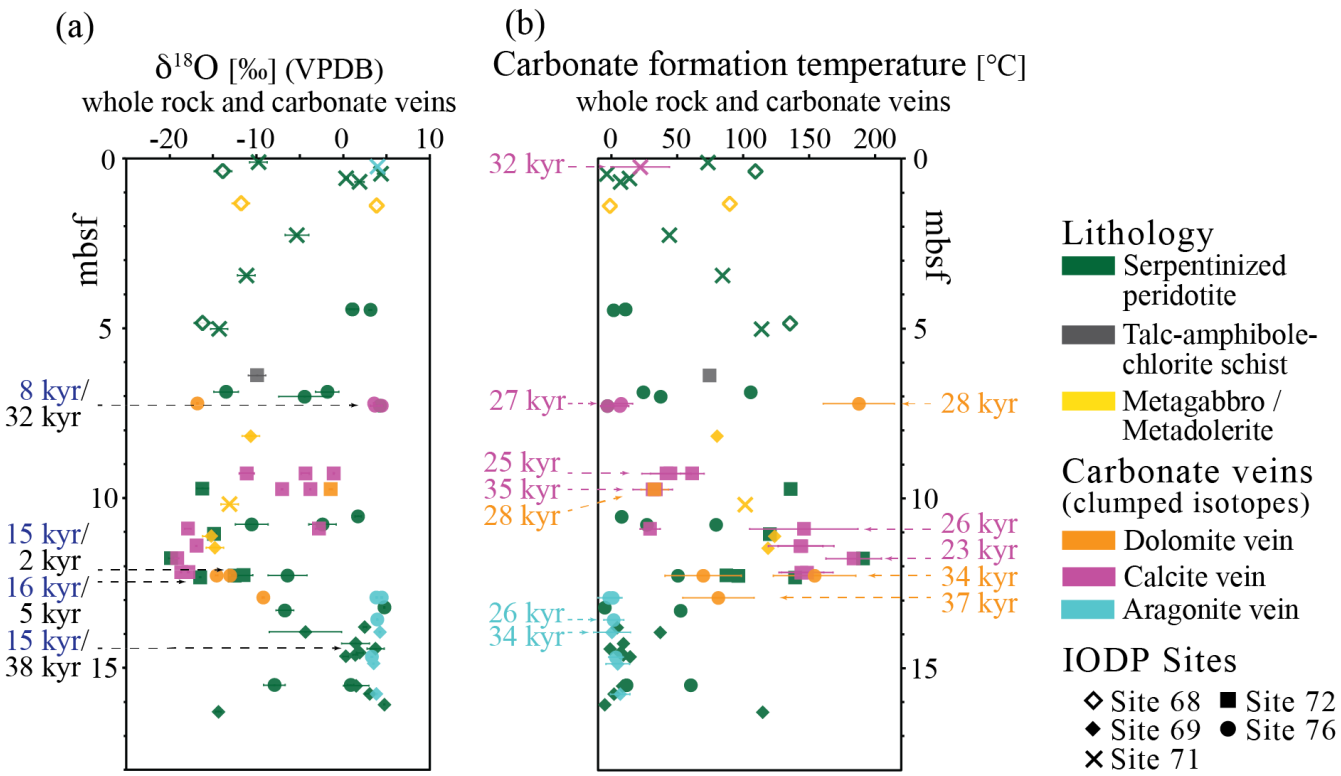

Figure 7. (a) $\delta^{18}O$ values and (b) variations in calculated carbonate precipitation temperature with depth below the seafloor (mbsf) of whole-rock samples and carbonate veins from the southern wall at the Atlantis Massif. Blue numbers indicate the ^{14}C ages (ka = kiloyears) of organic carbon, and the black numbers indicate ^{14}C ages of inorganic carbon from whole-rock samples. Radiocarbon ages of the vein carbonates are colour coded according to mineralogy.

Calculated oxygen isotope values of the fluid in equilibrium with the carbonates vary from -0.5 to +5.4 ‰. Circulating fluids in equilibrium with dolomite veins yield a range from -0.5 to +1.8 ‰. Calcite veins yield the most variable oxygen isotope values from -0.5 to +5.4‰, with a distinct separation between different sites. The fluids from Site M0072 have an average $\delta^{18}O$ of +0.2 ‰, whereas Site M0076 (avg. of +2 ‰) and M0071 ($\delta^{18}O$ = +5.4 ‰) have more ^{18}O-enriched values. The aragonite veins show similar to dolomite a restricted range of oxygen isotopic compositions with $\delta^{18}O_{Fluid}$ = +0.2 to +2.6 ‰.

4.4 Carbonate Types

The carbon and oxygen isotope composition of the carbonates allows distinguishing two groups of samples (Figure 6). Type I is characterized by ^{13}C- and ^{18}O-depleted carbon and oxygen compositions and corresponds to the bulk samples with low TIC concentrations. The calculated formation temperatures range from 49 to 191°C. Type II is characterized by higher TIC contents, with ^{13}C-enriched compositions and precipitation temperatures < 40°C. Some samples plot between the two groups suggesting a mixture of Type I and Type II.

4.5 Radiocarbon Dating

Radiocarbon ages were determined on four bulk rock samples, four dolomite, seven calcite and three aragonite veins, and five decarbonated bulk rocks (representing organic carbon) from the four sites (Table 3) and yielded ages from 38,393 to 1518 yr. Carbonate veins have ^{14}C ages ranging from 37,438 to 23,355 yr. The dated veins often contain multiple generations of carbonate, which could not be physically separated; therefore, the ^{14}C ages can represent a mixture of different generations. The dolomites gave the oldest ages from 37,438 to 27,745 yr, and a distinct increase in age with depth is observed at Hole M0076 (Figure 7b). Calcite ^{14}C ages range from 34,647 to 23,355 yr, which are slightly younger than the dolomites and show no distinct pattern across the sites (Table 3; Figure 8).

Table 3. Radiocarbon ages of carbonate veins in ultramafic rocks and whole rock sampels from the southern wall at the Atlantis Massif.

Site	Core			Interval (cm)		Depth (mbsf)		Type of the rock	Sample type			$F^{14}C$		^{14}C ages	
	Hole		Section	top	bot	top	bot		Mineral		Carbon type		σ (%)	(yr)	σ
71	A	1	1	0	5	0.58	0.63	Serpentinized dunite	Calcite	vein	inorganic	0.019	3.59	31902	339
69	A	9	2	57	61	13.94	13.98	Serpentinized harzburgite	Aragonite	vein	inorganic	0.014	3.66	34057	410
69	A	9	1	106	114	14.43	14.51	Serpentinized dunite	-	whole rock	total	0.017	4.45	32854	414
69	A	9	1	106	114	14.43	14.51	Serpentinized dunite	-	whole rock	organic	0.157	1.49	14886	116
69	A	9	1	106	114	14.43	14.51	Serpentinized dunite	-	whole rock	inorganic	0.008*		38393*	
72	B	7	1	28	30	9.27	9.29	Serpentinized dunite	Calcite	vein	inorganic	0.045	2.88	24928	246
72	B	7	1	75	77	9.74	9.76	Serpentinized dunite	Calcite	vein	inorganic	0.013	4.76	34647	595
72	B	7	1	75	77	9.74	9.76	Serpentinized dunite	Dolomite	vein	inorganic	0.029	2.89	28438	287
72	B	8	1	19	22	10.90	10.93	Serpentinized harzburgite	Calcite	vein	inorganic	0.040	3.09	25778	252
72	B	8	2	26	30	11.77	11.81	Serpentinized harzburgite	-	whole rock	organic	0.135	1.04	16103	119
72	B	8	2	26	30	11.77	11.81	Serpentinized harzburgite	Calcite	vein	inorganic	0.055	2.61	23355	224
72	B	8	CC	0	5	12.28	12.33	Serpentinized harzburgite	-	whole rock	total	0.489	1.00	5754	76
72	B	8	CC	0	5	12.28	12.33	Serpentinized harzburgite	-	whole rock	organic	0.155	1.45	14956	118
72	B	8	CC	0	5	12.28	12.33	Serp. harz. and talc/amphi. schist	-	whole rock	inorganic	0.828*		1518*	
72	B	8	CC	5	20	12.33	12.48	Serp. harz. and talc/amphi. schist	-	whole rock	total	0.478	0.70	5933	71
72	B	8	CC	5	20	12.33	12.48	Serpentinized harzburgite	-	whole rock	organic	0.136	1.65	16050	133
72	B	8	CC	5	20	12.33	12.48	Serpentinized harzburgite	-	whole rock	inorganic	0.523*		5208*	
76	B	5	1	48	50	7.21	7.23	Serpentinized dunite	Dolomite	vein	inorganic	0.032	2.84	27745	265
76	B	5	1	48	50	7.21	7.23	Serpentinized dunite	Calcite	vein	inorganic	0.034	3.48	27148	308
76	B	5	1	55	59	7.28	7.32	Serpentinized dunite	-	whole rock	total	0.030	3.05	28210	272
76	B	5	1	55	59	7.28	7.32	Serpentinized dunite	-	whole rock	organic	0.353	1.29	8355	100
76	B	5	1	55	59	7.28	7.32	Serpentinized dunite	-	whole rock	inorganic	0.019*		31919*	
76	B	5	1	55	59	7.28	7.32	Serpentinized dunite	Calcite	vein	inorganic	0.038	2.58	26202	211
76	B	8	1	112	117	12.27	12.32	Serpentinized harzburgite	Dolomite	vein	inorganic	0.015	1.79	33737	395
76	B	9	1	5	9	12.92	12.96	Serpentinized harzburgite	Dolomite	veine	inorganic	0.009	0.94	37438	578
76	B	9	1	5	9	12.92	12.96	Serpentinized harzburgite	Aragonite	vein	inorganic	0.047	2.53	24556	208
76	B	9	1	70	73	13.57	13.60	Serpentinized harzburgite	Aragonite	vein	inorganic	0.035	2.00	26822	226

* Calculated ages using mass balance, whole rock ages and carbon content of organic and inorganic component.

Aragonite veins range from 34,057 to 24,556 yr, with a clear distinction between old aragonite at Hole M0069A and younger aragonite at Hole M0076B (avg. ~26 kyr).

Total bulk carbon has a range of ^{14}C ages between 32,854 and 5,754 yr and is younger than the veins (Figure 7a). While samples from Hole M0069A and M0076B exhibit bulk rock ages in the range of the associated veins (~31 kyr), distinctly younger ages (~6 kyr) are measured in Hole M0072B. The radiocarbon ages of the bulk organic carbon (decarbonated samples) from all three central sites are much younger and more uniform (Table 3, Figure 8). $^{14}C_{TOC}$ ages range from 16,103 to 8355 yr, whereby the youngest age was measured at Hole M0076B. The fraction of modern carbon of the inorganic carbon were calculated by mass balance using radiocarbon ages and content of total carbon and total organic carbon. The ^{14}C ages of TIC range from 38,393 to 1,518 yr, and the estimated ages from Hole M0069A and M0076B coincide with ^{14}C ages from carbonate veins from the same hole. However, TIC ages from Hole M0072B have the youngest estimated ages (avg. 3,363 yr) and are distinctly different from the carbonate veins measured in that hole.

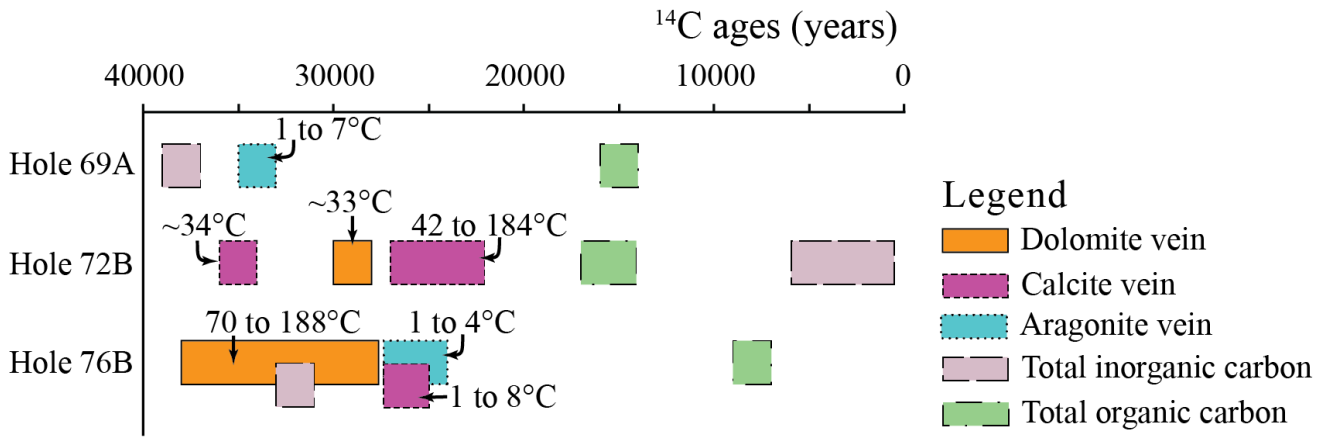

Figure 8. Schematic time-line of carbonate formation based on radiocarbon ages of carbonate veins, total inorganic-, and organic carbon from the three central Sites M0069A, M0072B and M0076B. Carbonate formation temperatures are based on clumped isotope investigation.

5 Discussion

Our data suggest at least three forms of carbonate precipitation in the basement rocks of the Atlantis Massif: (1) dispersed carbonization; (2) hydrothermal carbonate vein formation; and (3) aragonite and calcite precipitation in veins at ambient temperatures. These carbonates

allow critical new insights into fluid flow and mass transfer within a serpentinite-hosted hydrothermal system. In the following, we discuss the evolution of carbonate formation in the AM and then discuss the implications for organic carbon storage in the oceanic crust.

5.1 Continuous Dispersed Carbonate Precipitation

Initial alteration of the AM is characterized by pervasive serpentinization, which leads to the formation of serpentine mesh textures after olivine at temperatures between 200 to 350°C, as is commonly observed in diverse geodynamic contexts (Rouméjon, Früh-Green, et al., 2018). The water is supplied via a fine network along grain boundaries, which leads to the formation of the earliest Type I carbonates with progressive hydration and cooling of the basement at temperatures from 190 to 50°C (Figure 9a). These formation temperatures are calculated from bulk rock $^{18}O_{TIC}$ compositions and may represent a mixture of even higher (T < 250°C, Frost & Beard, 2007) and lower formation temperatures. Dispersed carbonates are found throughout the southern wall. Radiocarbon ages indicate precipitation has continued from over 38 kyr ago to 1.5 kyr locally at the central sites, suggesting that dispersed carbonate formation is associated with progressive hydrothermal circulation and serpentinization of the AM and is likely still active at shallow crustal levels (Figure 8). This hypothesis is consistent with the results of Proskurowski et al. (2008), who showed that DIC concentrations in the Lost City vent fluids are extremely low and suggested that serpentinization and carbonization are on-going processes.

Type I carbonates have a distinct isotopic signature indicating a ^{13}C-depleted DIC source (Figure 6). Highly depleted ^{13}C compositions are typical for organic carbon; and in submarine low-temperature hydrothermal systems, two sources for ^{13}C-depleted DIC are possible: (1) biologically mediated respiration of organic matter (OM) and (2) abiotic hydrothermal degradation of DOM from seawater-derived fluids. A third less depleted, but relatively light carbon source is magmatic volatiles (CH_4, CO_2) trapped in plutonic and mantle rocks. CO_2 and HCO_3^- can be actively produced from organisms living within the ultramafic and mafic rocks or can be produced by biologically mediated respiration of OM, transported via the circulating fluid and stored in the basement rocks. Recent microbiological and metagenomic studies indicate that microbial life can be sustained within the lithosphere and provide evidence that microbial utilization of H_2, CH_4 and formate may be common in different serpentinization systems (e.g., Brazelton et al., 2012; Lang et al., 2018; Schrenk et al., 2013). Furthermore, micron-scale organic matter has been detected encapsulated in serpentinized peridotites at sites along the Mid-Atlantic Ridge (Ménez et al., 2012, 2018). Motamedi et al.

(2020) were able to identify Thermoplasmata, Acidobacteria, Acidimicrobia and Chloroflexi as organisms potentially living within the ultramafic rocks at the AM. However, the currently known temperature limit for life is 122°C (Takai et al., 2008), and our results show that Type I carbonates precipitated at temperatures up to 191°C, well above this limit. Therefore, we propose that biologically mediated respiration of OM within the basement is unlikely as a carbon source for Type I carbonates or only contributes a minor amount of ^{13}C-depleted carbon.

Another possible source for ^{13}C- depleted DIC is the abiotic hydrothermal decay of DOM transported into the rocks by circulating seawater. Part of marine DOM is known to be very stable in deep ocean water and is mostly unaffected by consumption, oxidation and reactive surface processes over long periods of time, as indicated by an average DOM age of 4,000 to 6,400 ^{14}C years (Druffel & Griffin, 2015; Flerus et al., 2012). One possible way to remove the oldest and most recalcitrant forms of DOM from seawater is thermal degradation during hydrothermal alteration of the oceanic crust (Hawkes et al., 2015; Lang et al., 2006; McCollom & Seewald, 2003; Seewald, 2001). The presence of organic compounds such as isoprenoids (pristane, phytane and squalene), polycyclic compounds (hopanes and steranes), and higher abundances of n-C16 to n-C20 alkanes at the central dome of the Atlantis Massif down to 1095 mbsf (IODP Site U1309) implies seawater circulation and transport of DOM deep into the basement (Delacour, Früh-Green, Bernasconi, Schaeffer, et al., 2008). In these environments, abiotic oxidation of DOM by water, nitrate, sulphate and oxidized minerals (Bischoff & Seyfried, 1978; McCollom & Seewald, 2003; Seewald, 2001; Zhang et al., 2007) followed by decarboxylation (McCollom & Seewald, 2003; Seewald, 2001) can lead to a stepwise decrease in molecular weight of DOM, production of ^{13}C-depleted CO_2 and CH_4 and, ultimately, the removal of DOM from solution (McCollom & Seewald, 2003). Hawkes et al. (2015, 2016) and Rossel et al. (2017) recently performed hydrothermal experiments with marine DOM using fluid samples from nine different vent fields of the Atlantic, Pacific and the Southern Ocean to study abiotic degradation of solid-phase extractable DOM in a temperature range from 100°C to 380°C. These studies indicate that the vast majority of solid-phase extractable DOM cannot survive hydrothermal circulation at temperatures > 380°C. At temperatures between 100°C and 200°C, only some low-molecular-weight, oxygen-depleted and heteroatom (N, S, P) species may survive. Extrapolation of their data suggests that substantial alteration of DOM may start at 68°C ± 14°C (Hawkes et al., 2015, 2016). Our results indicate a minimum temperature of 50 to 190°C, which is sufficiently elevated for the efficient degradation of solid-phase extractable-DOM. Thus, we argue that the abiotic hydrothermal

decay of DOM very likely occurs during circulation of the hydrothermal fluid within the AM basement and that this carbon source is the main input for Type I carbonate formation.

A subset of Type I carbonates is characterized by $\delta^{13}C$ between -5.0 and -2.1 ‰. For this range of compositions, lighter mantle CO, CO_2, or CO_2 derived from the oxidation of CH_4 and other short-chain hydrocarbons released from fluid inclusions is an additional possible DIC source. Mantle carbon has a bimodal range with $\delta^{13}C$ clustering around -5 and -25 ‰ (Deines, 2002). Thus, ^{13}C-depleted carbon derived from volatiles leached from the mafic and ultramafic basement sequences is potentially an additional carbon source for Type I carbonates. Methane observed in fluid inclusions in the Southwest Indian Ridge plutonic rocks is characterized by $\delta^{13}C$ of -10 to -30 ‰ (Kelley, 1996; Kelley et al., 2002; Kelley & Früh-Green, 1999, 2001), a range that matches the composition of methane measured at the Lost City vents (-16 to -9 ‰; Proskurowski et al., 2008), as well as other hydrothermal systems such as the Von Damm field at the Cayman Rise (CH_4 = -15.4 ‰; McDermott et al., 2015) where magmatic volatile-rich fluid inclusions are suggested to be a source of methane. In addition, CH_4 at the LCHF is radiocarbon free (Proskurowski et al., 2008), which is consistent with the interpretation that CH_4 and other reduced carbon phases are derived from volatile-rich fluid inclusions in the AM basement.

Carbonates occur in the cores of fully serpentinized olivines. The sizes of these carbonates are, in general, < 20 μm, which is too small for *in-situ* isotope investigations. Thus, we can only assume that the carbonates in the olivine cores are part of the dispersed carbonates and lead to the depleted whole-rock ^{13}C values. Assuming that abiotic alteration of organic matter is the main source of ^{13}C-depleted carbon and that organic matter is preferentially stored within the serpentine mesh cores replacing olivine, it is possible that *in-situ* oxidation of OM creates low molecular weight organic acids and in the end decays, with mineral catalysis, to form ^{13}C-depleted CO_2 and CH_4 within the serpentine mesh cores. These compounds could be further oxidized and react with Ca^{2+} and Mg^{2+} to form carbonates. A higher concentration of organic compounds inside cores of serpentinite mesh textures has been previously reported by Plümper et al. (2017) and Ménez et al. (2018) from the South Chamorro Mud Volcano (Izu-Bonin-Mariana subduction zone) and the central dome of the Atlantis Massif, respectively. Thus, it is likely that carbonates precipitating in various hydrothermal systems can preserve clear isotopic signatures of organic matter decay for long periods of time and may be an important aspect to fully understand the fate of organic carbon in hydrothermal systems.

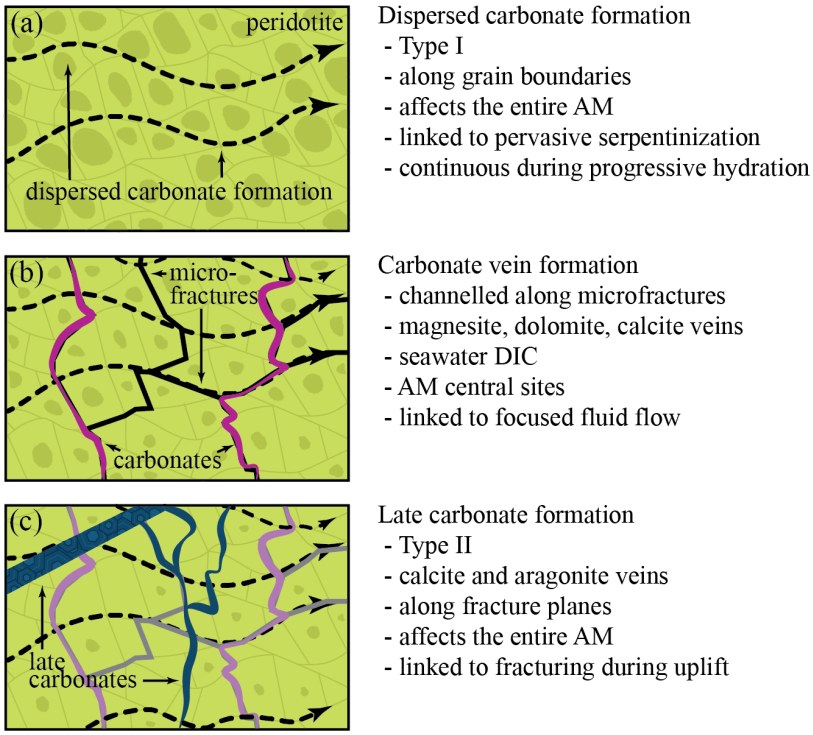

Figure 9. Schematic sketch illustrating the sequence of hydration and carbonation processes affecting mantle rocks at the Atlantis Massif. See text for detailed discussion.

5.2 Carbonate Precipitation during Progressive Focused Fluid Flow

As the footwall reaches shallow crustal levels, fluid flow is dominated by continuous fracture planes and microfacturing caused by serpentinization, which form permeability pathways and channel the fluids along specific domains of the mesh-textured serpentinites (Rouméjon, Früh-Green, et al., 2018). Serpentinization shows a transition from pervasive to localized, as indicated by recrystallization of the mesh texture to chrysotile-dominated and banded veins (Rouméjon, Früh-Green, et al., 2018). Our studies indicate that focused fluid flow leads to the formation of carbonate veins in the central part of the AM at temperatures between 30 and 188°C depending on the location (Figure 9b). High-temperature dolomite veins ($T_{\Delta 47}$ = 70 to 188°C) are found closest to the LCHF, whereas the other central site shows a distinction between shallow ($T_{\Delta 47}$ ~40°C) and deeper calcites ($T_{\Delta 47}$ ~152°C), indicating locally distinct and variable fluid circulation. A change from pervasive to localized and focused fluid flow at the central sites is consistent with previous work from Boschi et al. (2006), Karson et al.(2006) and Kelley et al. (2005), who proposed that the currently active venting at Lost City is

controlled by steeply dipping normal faults striking parallel to the regional trend of the ATF and parallel to the MAR. These normal faults allowed deeper fluid circulation and serpentinization beneath that area of the massif and channelled upward flow through the LCHF. The carbonate veins δ^{13}C from -3.0 to +0.2 ‰ are less ^{13}C-depleted than Type I carbonates (Figure 6), which suggests a dominance of DIC derived from seawater with minor contributions of ^{13}C- depleted carbon from magmatic volatiles and/or degradation of DOC. Alternatively, the more ^{13}C-depleted carbonate veins could also be explained by Rayleigh distillation of the DIC in the fluid caused by progressive precipitation of carbonate. Assuming precipitation from seawater DIC (δ^{13}C = 0 ‰) and a fractionation factor between DIC and calcite of 2 ‰ (i.e. with the calcite being 2 ‰ heavier than the DIC), removal of about 90% of the original seawater results in a residual DIC in solution with a δ^{13}C of approximately -5 ‰. This residual DIC would result in precipitation of carbonates with δ^{13}C = ~-3 ‰, which is within the range observed in the carbonate veins.

The radiocarbon ages from 37 to 23 kyr (Figure 8) confirms previously reported ^{14}C ages for the LCHF carbonate towers and veins from Früh-Green et al. (2003), who showed that hydrothermal activity started at least 30 kyr ago. If we consider that Ludwig et al. (2011) reported much older U/Th ages of the oldest LCHF chimneys of 120 kyr, it is possible that the ^{14}C ages could also represent a mixture of carbonates precipitated > 37 kyr ago and younger (or modern) carbonate. This is consistent with results from Proskurowski et al. (2008), who showed that the LCHF vent fluids have very low carbonate contents and argued that on-going intensive carbonate formation within the basement leads to DIC removal. It is likely that carbonate precipitation associated with extensive focused fluid flow has occurred over a longer period of time than that indicated by the radiocarbon ages and is likely an on-going process in deeper areas below the LCHF.

5.3 Late-stage, Fracture-controlled Carbonate Formation

As the Atlantis Massif was progressively extended, unroofed and uplifted, late-stage normal faults formed and created new hydration pathways along brittle fault planes. Underwater camera imagery shows that brittle deformation is widespread along the southern wall of the AM, indicating that a series of faults, rather than a single detachment, accommodated the uplift displacement (Blackman et al., 2002; Karson et al., 2006). Microstructural analysis shows that brittle deformation is concentrated in a section within the 50-100 m below the sedimentary cover of the massif (Karson et al., 2006). It is possible that

continued circulation of fluids as the massif was uplifted and cooled has led to calcite and aragonite veins at temperatures < 40°C and Type II carbonates in the bulk rock (Figure 9c). This late-stage carbonate formation increases near the summit of the massif and throughout the southern wall and possibly throughout the entire AM.

Type II carbonates have carbon isotope signatures similar to those in carbonate veins that form during this late stage (Figure 6). This suggests that DIC from seawater is the dominant carbon source and that the fluid represents fairly unmodified seawater that only interacted with the basement to a low degree. Calculated δ^{18}O of the fluids in equilibrium with the vein carbonates are ~+1.4 ± 2 ‰, which is identical to seawater and provides additional evidence that seawater bicarbonate is the main carbon source. Late-stage aragonite precipitation at ambient temperatures is a common feature of shallower parts of submarine hydrothermal systems and has been previously described by Alt & Shanks (1998) and Blusztajn & Hart (1996).

Summarizing, the formation of dispersed carbonates represented the first carbonization phase and occurred at temperatures of 50 to 190°C, with a ^{13}C-depleted carbon source likely derived from the abiotic hydrothermal decomposition of dissolved organic matter (DOM). Dispersed precipitation of carbonate in the basement progressed with continuous hydration of the AM until at least 1500 yr ago. This is followed by dolomite, magnesite and calcite precipitation in veins, associated with focused fluid flow at temperatures between 30 and 188°C, and seawater DIC as the dominant carbon source. These carbonates exhibit ^{14}C ages from approximately 37 to 23 kyr and are characterized by variable carbon isotope signatures following a Rayleigh distillation trend. Late-stage precipitation of aragonite and calcite in veins under ambient temperatures was likely driven by seawater circulation during uplift and progressive brittle fracturing of the massif.

5.4 Serpentinites as a Potential Sink for Marine DOC?

Recent studies have provided evidence that the ultramafic basement can sustain microbial life (Barry et al., 2019; Colman et al., 2017; Fullerton et al., 2019), and the carbon isotope composition of carbonates from this study show that ^{13}C depleted, potentially organic carbon, is a significant carbon source in the system. In general, the TOC content of oceanic serpentinites is highly variable. Compilation of data from Hess Deep, MARK, SWIR, Caiman Rise, Iberian Margin, Vema FZ, Atlantis Massif, Mariana and the Tyrrhenian Sea of Früh-Green et al. (2004, reference therein) showed that TOC ranges from 30 to 2700 ppm in oceanic

ultramafic and 20 to 1000 ppm in mafic rocks. The highest TOC contents measured in our study is ~800 ppm in the ultramafic rocks, ~500 ppm in talc-amphibole-chlorite schists, and ~250 ppm in the gabbroic rocks. No clear distinctions in concentrations of organic carbon are observed between the mafic and ultramafic rocks (Figure 5b), which indicates that the pervasive fluid flow associated with dispersed carbonate precipitation throughout the AM is likely the main mechanism of DOC transport. Thus, we hypothesize that abiotic hydrothermal decay of DOM and pervasive fluid flow leads to the ^{13}C-depleted carbon of Type I carbonates, and more focused fluid flux only has a minor influence on TOC content.

The isotopic composition of TOC in the serpentinites from the AM ($\delta^{13}C_{TOC}$ = -28.3 to -19.8 ‰) coincides only in part with the average δ^{13}C of DOC of the North Atlantic which ranges from -23.1 to -22.2 ‰ (Eadie et al., 1978; Jeffrey, 1969). The samples with lower δ^{13}C can be affected by preferential removal of compounds enriched in ^{13}C or could have a contribution from another more ^{13}C-depleted source of organic carbon. Delacour, Früh-Green, Bernasconi, Schaeffer, et al. (2008) suggested a mixture of dissolved or particulate organic carbon from seawater circulation combined with minor *in-situ* production through the microbial activity as the TOC source in the gabbroic rocks from the central dome of the AM. Motamedi et al. (2020) were able to determine microbial groups that may live within the basement of the AM and lead to *in-situ* production of organic carbon. However, in our study, serpentinized peridotites and talc-amphibole-chlorite schists with the highest TOC content are located at the central Site M0072, which is characterized by high calcite formation temperatures ($T_{\Delta 47, max}$ = 184°C) that are above the currently known temperature limit for life of 122°C (Takai et al., 2008). This observation makes *in-situ* production of organic carbon compounds at Site M0072 during carbonate formation unlikely but does not exclude its formation at other locations and later transport to the central sites or *in-situ* production after carbonate formation.

The average radiocarbon age of TOC in the serpentinized peridotites is 14 kyr, which is younger than the carbonates and suggests that older DOM is largely decomposed or may be incorporated in Type I carbonates, and only younger and more recently transported DOM is present as TOC in the rocks. One exception is the dispersed Type I carbonates from the central Site M0072 that yielded an average age of ~3 kyr, which is younger than the TOC at the same site ($^{14}C_{TOC, M0072B}$ = ~15.5 kyr) (Figure 8). This suggests that thermal degradation of DOM and incorporation of the resulting carbon in carbonates is still on-going and that the radiocarbon ages of TOC are best explained by a mixture of old DOC, which survives hydrothermal

decomposition, and young DOC. The preservation and subsequent leaching of potentially old organic carbon from the basement is supported by recent studies of Lang et al. (2010, 2012), which found that DOC concentration in the vent fluids is almost twice as high as those from the seawater. However, the effect of DIC and DOC removal from the oceanic reservoir is not well constrained, and the mechanisms of DOC removal are not well understood (Hansell, 2002).

Our data can be considered to estimate carbon fixation in the oceanic crust. To do this, we use a crustal production rate of $6.0 \pm 0.8 \times 10^{16}$ g/yr calculated by Mottl (2003) and assume that approximately 20 – 25 % of the oceanic crust is composed of serpentinized peridotites (Cannat, 1995) so that only 5 % of the new seafloor produced per year is composed of ultramafic rocks (Bach et al., 2001). This results in annual storage rates of up to 1.7×10^{11} mol C/yr of organic carbon (avg. 7×10^{10} mol C/yr) and up to 6×10^{12} mol C/yr of inorganic carbon (avg. 1×10^{12} mol C/yr), assuming organic carbon contents from 39 to 700 ppm and inorganic carbon contents from 14 ppm to 2.4 wt%. Former studies from Alt & Teagle (1999) and Staudigel et al. (1989) estimated storage rates for inorganic carbon of up to 2.7×10^{12} mol C/yr, which is approximately half indicated by our study. Delacour, Früh-Green, Bernasconi, Schaeffer, et al. (2008) reported up to 1.2×10^{11} mol C/yr for annual storage rates of organic carbon within the oceanic crust, which coincides with results of our studies, and Lang et al. (2006) calculated a global DOC loss of up to 1.2×10^{9} mol C/yr through high-temperature axial vents, which accounts for less than 2% of the ~14 μM DOC loss during deep oceanic circulation. In comparison, our calculation shows 60 times higher DOC removal, which would explain more than the assumed ~14 μM DOC loss. Thus, moderate temperature and off-axis hydrothermal systems potentially represent an important sink for inorganic carbon and a significant sink for organic carbon compared to high-temperature axis vents.

6. Conclusions

This study contributes new data on the geochemistry of inorganic and organic carbon in oceanic serpentinites and gabbroic rocks and provides constraints on the fate of dissolved carbon in seawater during long-lived serpentinization and hydrothermal alteration of the oceanic lithosphere.

The isotopic investigations point to three sources of inorganic carbon: (1) abiotic hydrothermal degradation of dissolved organic matter; (2) seawater; and (3) mantle volatiles. The relatively ^{13}C-depleted composition of the organic carbon points to a dominant marine

origin with a possible minor component from *in-situ* production through microbial activity. Although the biotic formation of TOC within the basement of the AM would be possible, there is no clear evidence for significant biological activity in the serpentinites. In contrast, the high carbonate formation temperatures probably inhibited microbial activity. We propose that a high degree of seawater influx channelled below the central part of the southern wall likely favours the transport of marine DOC and DIC into the serpentinites and dominates carbonization at least for the past 38,000 years. Dispersed carbonates record initial carbonization during the earlier stages of serpentinization and is progressively deposited during continuous hydration and alteration of the oceanic core complex and can record an isotopic signature of dissolved organic matter decay over geological eras. Thus, our study suggests that serpentinites in moderate temperature off-axis hydrothermal systems are important for storage of marine DIC and may represent a more significant sink of DOC from seawater than high-temperature vent systems at mid-ocean ridges.

Moderate-temperature, off-axis hydrothermal vent systems are crucial to better understand the impact of seawater circulation through the oceanic crust on the global carbon budget, and further investigations on oceanic serpentinites and gabbros are necessary to better constrain the amount of carbon removed through deep seawater circulation in the oceanic crust. Furthermore, several authors (Holm et al., 1992, 2006; Martin & Russell, 2007; Shock, 1990; Shock & Schulte, 1998) propose that abiotic formation of organic compounds necessary for early life requires alkaline conditions and high H_2 contents in the hydrothermal fluids. Hydration and serpentinization of mantle peridotites produce these type of conditions; thus, further studies of the transport, transformation and storage of carbon in these systems will not only help to better evaluate the potential of mantle rocks to store carbon and reduce CO_2 emission in the future but may also provide information to better evaluate the conditions of emergence of life on Earth.

Acknowledgements

We would like to thank Madalina Jaggi, Negar Haghipour, Stewart Bishop and Lydia Zehnder for help with sample preparation and analyses, as well as the European Consortium for Ocean Research Drilling (ECORD) and the IODP Expedition 357 science party for providing drill core samples for this study. We gratefully acknowledge funding by the Swiss National Science Foundation (SNF) project No. 200021_163187 to Früh-Green. Results of individual analyses of the samples will be available online on PANGAEA (www.pangaea.de).

References

Abrajano, T. A., Sturchio, N. C., Kennedy, B. M., Lyon, G. L., Muehlenbachs, K., & Bohlke, J. K. (1990). Geochemistry of reduced gas related to serpentinization of the Zambales ophiolite, Philippines. *Applied Geochemistry*, *5*(5–6), 625–630. https://doi.org/10.1016/0883-2927(90)90060-I

Alt, J. C., & Shanks, W. C. (1998). Sulfur in serpentinized oceanic peridotites: Serpentinization processes and microbial sulfate reduction. *Journal of Geophysical Research: Solid Earth*, *103*(B5), 9917–9929. https://doi.org/10.1029/98jb00576

Alt, J. C., & Teagle, D. A. H. (1999). The uptake of carbon during alteration of ocean crust. *Geochimica et Cosmochimica Acta*, *63*(10), 1527–1535. https://doi.org/10.1016/S0016-7037(99)00123-4

Alt, J. C., Shanks, W. C., Crispini, L., Gaggero, L., Schwarzenbach, E. M., Früh-Green, G. L., & Bernasconi, S. M. (2012). Uptake of carbon and sulfur during seafloor serpentinization and the effects of subduction metamorphism in Ligurian peridotites. *Chemical Geology*, *322–323*, 268–277. https://doi.org/10.1016/j.chemgeo.2012.07.009

Bach, W., Alt, J. C., Niu, Y., Humphris, S. E., Erzinger, J., & Dick, H. J. B. (2001). The geochemical consequences of late-stage low-grade alteration of lower ocean crust at the SW Indian Ridge: results from ODP Hole 735B (Leg 176). *Geochimica et Cosmochimica Acta*, *65*(19), 3267–3287. https://doi.org/10.1016/S0016-7037(01)00677-9

Bach, W., Rosner, M., Jöns, N., Rausch, S., Robinson, L. F., Paulick, H., & Erzinger, J. (2011). Carbonate veins trace seawater circulation during exhumation and uplift of mantle rock: Results from ODP Leg 209. *Earth and Planetary Science Letters*, *311*(3–4), 242–252. https://doi.org/10.1016/j.epsl.2011.09.021

Barbieri, M., Masi, U., & Tolomeo, L. (1979). Stable isotope evidence for a marine origin of ophicalcites from the north-central Apennines (Italy). *Marine Geology*, *30*(3–4), 193–204. https://doi.org/10.1016/0025-3227(79)90015-X

Barnes, I., & O'Neil, J. R. (1969). The relationship between fluids in some fresh alpine-type ultramafics and possible modern serpentinization, western United States. *Bulletin of the Geological Society of America*, *80*(10), 1947–1960. https://doi.org/10.1130/0016-7606(1969)80[1947:TRBFIS]2.0.CO;2

Barnes, I., Rapp, J. B., O'Neil, J. R., Sheppard, R. A., & Gude, A. J. (1972). Metamorphic assemblages and the direction of flow of metamorphic fluids in four instances of serpentinization. *Contributions to Mineralogy and Petrology*, *35*(3), 263–276. https://doi.org/10.1007/BF00371220

Barry, P. H., de Moor, J. M., Giovannelli, D., Schrenk, M. O., Hummer, D. R., Lopez, T., et al. (2019). Forearc carbon sink reduces long-term volatile recycling into the mantle. *Nature*, *568*(7753), 487–492. https://doi.org/10.1038/s41586-019-1131-5

Bernasconi, S. M., Müller, I. A., Bergmann, K. D., Breitenbach, S. F. M., Fernández, Á., Hodell, D. A., et al. (2018). Reducing Uncertainties in Carbonate Clumped Isotope Analysis Through Consistent Carbonate-Based Standardization. *Geochemistry, Geophysics, Geosystems*, *19*(9), 2895–2914. https://doi.org/10.1029/2017GC007385

Bischoff, J. L., & Seyfried, W. E. (1978). Hydrothermal Chemistry of Seawater from 25° to 350°C. *American Journal of Science*, *278*, 838–860.

Blackman, D. K., Cann, J. R., Janssen, B., & Smith, D. K. (1998). Origin of extensional core complexes: Evidence from the Mid-Atlantic Ridge at Atlantis Fracture Zone. *Journal of Geophysical Research: Solid Earth*, *103*(B9), 21315–21333. https://doi.org/10.1029/98jb01756

Blackman, D. K., Karson, J. A., Kelley, D. S., Cann, J. R., Früh-Green, G. L., Gee, J. S., et al. (2002). Geology of the Atlantis Massif (Mid-Atlantic Ridge, 30° N): Implications for the evolution of an ultramafic oceanic core complex. *Marine Geophysical Researches*, *23*(5/6), 443–469. https://doi.org/10.1023/B:MARI.0000018232.14085.75

Blusztajn, J. S., & Hart, S. R. (1996). Sr and O Isotopic Ratios of Aragonite Veins from Site 895. *Proceedings of the Ocean Drilling Program, 147 Scientific Results*, *147*, 311–313. https://doi.org/10.2973/odp.proc.sr.147.035.1996

Bonatti, E., Lawrence, J. R., Hamlyn, P. R., & Breger, D. (1980). Aragonite from deep sea ultramafic rocks. *Geochimica et Cosmochimica Acta*, *44*(8), 1207–1214. https://doi.org/10.1016/0016-7037(80)90074-5

Boschi, C., Früh-Green, G. L., Delacour, A., Karson, J. A., & Kelley, D. S. (2006). Mass transfer and fluid flow during detachment faulting and development of an oceanic core complex, Atlantis Massif (MAR 30°N). *Geochemistry, Geophysics, Geosystems*, *7*(1). https://doi.org/10.1029/2005GC001074

Boschi, C., Dini, A., Früh-Green, G. L., & Kelley, D. S. (2008). Isotopic and element exchange during serpentinization and metasomatism at the Atlantis Massif (MAR 30°N): Insights from B and Sr isotope data. *Geochimica et Cosmochimica Acta*, *72*(7), 1801–1823. https://doi.org/10.1016/j.gca.2008.01.013

Brazelton, W. J., Schrenk, M. O., Kelley, D. S., & Baross, J. A. (2006). Methane- and sulfur-metabolizing microbial communities dominate the lost city hydrothermal field ecosystem. *Applied and Environmental Microbiology*, *72*(9), 6257–6270. https://doi.org/10.1128/AEM.00574-06

Brazelton, W. J., Nelson, B., & Schrenk, M. O. (2012). Metagenomic evidence for H2 oxidation and H2 production by serpentinite-hosted subsurface microbial communities. *Frontiers in Microbiology*, *2*(JAN), 1–16. https://doi.org/10.3389/fmicb.2011.00268

Breitenbach, S. F. M., & Bernasconi, S. M. (2011). Carbon and oxygen isotope analysis of small carbonate samples (20 to 100 μg) with a GasBench II preparation device. *Rapid Communications in Mass Spectrometry*, *25*(13), 1910–1914. https://doi.org/10.1002/rcm.5052

Cann, J. R., Blackman, D. K., Smith, D. K., McAllister, E., Janssen, B., Mello, S., et al. (1997). Corrugated slip surfaces formed at ridge–transform intersections on the Mid-Atlantic Ridge. *Nature*, *385*(6614), 329–332. https://doi.org/10.1038/385329a0

Cannat, M. (1995). Thin crust, ultramafic exposures, and rugged faulting patterns at the Mid-Atlantic Ridge (22°-24°N). *Geology*, *23*(1), 49–52. https://doi.org/10.1130/0091-7613(1995)023<0049:TCUEAR>2.3.CO;2

Cannat, M., Fontaine, F., & Escartín, J. (2010). Serpentinization and associated hydrogen and methane fluxes at slow-spreading ridges. In *Diversity of Hydrothermal Systems on Slow Spreading Ocean Ridges* (pp. 241–264). https://doi.org/10.1029/2008GM000760

Carlson, R. L. (2001). The abundance of ultramafic rocks in Atlantic Ocean crust. *Geophysical Journal*, *144*(1), 37–48.

Charlou, J. L., Donval, J. P., Fouquet, Y., Jean-Baptiste, P., & Holm, N. G. (2002). Geochemistry of high H2 and CH4 vent fluids issuing from ultramafic rocks at the Rainbow hydrothermal field (36°14′N, MAR). *Chemical Geology*, *191*(4), 345–359. https://doi.org/10.1016/S0009-2541(02)00134-1

Charlou, J. L., Donval, J. P., Konn, C., Ondréas, H., Fouquet, Y., Jean-Baptiste, P., & Fourré, E. (2010). High production and fluxes of H2 and CH4 and evidence of abiotic hydrocarbon synthesis by serpentinization in ultramafic-hosted hydrothermal systems on the Mid-Atlantic Ridge. In *Diversity of Hydrothermal Systems on Slow Spreading Ocean Ridges* (pp. 265–296). https://doi.org/10.1029/2008GM000752

Coggon, R. M., Teagle, D. A. H., Cooper, M. J., & Vanko, D. A. (2004). Linking basement carbonate vein compositions to porewater geochemistry across the eastern flank of the Juan de Fuca Ridge, ODP Leg 168. *Earth and Planetary Science Letters*, *219*(1–2), 111–128. https://doi.org/10.1016/S0012-821X(03)00697-6

Colman, D. R., Poudel, S., Stamps, B. W., Boyd, E. S., & Spear, J. R. (2017). The deep, hot biosphere: Twenty-five years of retrospection. *Proceedings of the National Academy of Sciences of the United States of America*, *114*(27), 6895–6903. https://doi.org/10.1073/pnas.1701266114

Curtis, A. C., Wheat, C. G., Fryer, P., & Moyer, C. L. (2013). Mariana Forearc Serpentinite Mud Volcanoes Harbor Novel Communities of Extremophilic Archaea. *Geomicrobiology Journal*, *30*(5), 430–441. https://doi.org/10.1080/01490451.2012.705226

Deines, P. (2002). The carbon isotope geochemistry of mantle xenoliths. *Earth-Science Reviews*, *58*(3–4), 247–278. https://doi.org/10.1016/S0012-8252(02)00064-8

Delacour, A., Früh-Green, G. L., Bernasconi, S. M., Schaeffer, P., & Kelley, D. S. (2008). Carbon geochemistry of serpentinites in the Lost City Hydrothermal System (30°N, MAR). *Geochimica et Cosmochimica Acta*, *72*(15), 3681–3702. https://doi.org/10.1016/j.gca.2008.04.039

Delacour, A., Früh-Green, G. L., Bernasconi, S. M., & Kelley, D. S. (2008). Sulfur in peridotites and gabbros at Lost City (30°N, MAR): Implications for hydrothermal alteration and microbial activity during serpentinization. *Geochimica et Cosmochimica Acta*, *72*(20), 5090–5110. https://doi.org/10.1016/j.gca.2008.07.017

Detrick, R. S., & Collins, J. A. (1998). Seismic structure of ultramafics exposed at shallow crustal levels in the Mid-Atlantic Ridge rift valley at 15°N. *Eos Trans. AGU*, *79*(45), Fall Meet. Suppl., F800.

Druffel, E. R. M., & Griffin, S. (2015). Radiocarbon in dissolved organic carbon of the South Pacific Ocean. *Geophysical Research Letters*, *42*(10), 4096–4101. https://doi.org/10.1002/2015GL063764

Eadie, B. J., Jeffrey, L. M., & Sackett, W. M. (1978). Some observations on the stable carbon isotope composition of dissolved and particulate organic carbon in the marine environment. *Geochimica et Cosmochimica Acta*, *42*(8), 1265–1269. https://doi.org/10.1016/0016-7037(78)90120-5

Ehlmann, B. L., Mustard, J. F., & Murchie, S. L. (2010). Geologic setting of serpentine deposits on Mars. *Geophysical Research Letters*, *37*(6), n/a-n/a. https://doi.org/10.1029/2010gl042596

Eickmann, B., Bach, W., & Peckmann, J. (2009). Authigenesis of carbonate minerals in modern and Devonian ocean-floor hard rocks. *Journal of Geology*, *117*(3), 307–323. https://doi.org/10.1086/597362

Etiope, G., & Sherwood Lollar, B. (2013). Abiotic methane on earth. *Reviews of Geophysics*, *51*(2), 276–299. https://doi.org/10.1002/rog.20011

Fernández, Á., Müller, I. A., Rodríguez-Sanz, L., van Dijk, J., Looser, N., & Bernasconi, S. M. (2017). A Reassessment of the Precision of Carbonate Clumped Isotope Measurements: Implications for Calibrations and Paleoclimate Reconstructions. *Geochemistry, Geophysics, Geosystems*, *18*(12), 4375–4386. https://doi.org/10.1002/2017GC007106

Flerus, R., Lechtenfeld, O. J., Koch, B., McCallister, S. L., Schmitt-Kopplin, P., Benner, R., et al. (2012). A molecular perspective on the ageing of marine dissolved organic matter. *Biogeosciences*, *9*(6), 1935–1955. https://doi.org/10.5194/bg-9-1935-2012

Friedman, I., & O'Neil, J. R. (1977). Compilation of stable isotope fractionation factors of geochemical interest. In: Fleisher, M. (Ed.), Data of Geochemistry, 6th ed. *Geological Survey Professional Paper*, *440*, 1–12. https://doi.org/10.1016/S0016-0032(20)90415-5

Frost, R. B., & Beard, J. S. (2007). On silica activity and serpentinization. *Journal of Petrology*, *48*(7), 1351–1368. https://doi.org/10.1093/petrology/egm021

Früh-Green, G. L., Kelley, D. S., Bernasconi, S. M., Karson, J. A., Ludwig, K. A., Butterfield, D. A., et al. (2003). 30,000 Years of Hydrothermal Activity at the Lost City Vent Field. *Science*, *301*(5632), 495–498. https://doi.org/10.1126/science.1085582

Früh-Green, G. L., Connolly, J. A. D., Plas, A., Kelley, D. S., & Grobéty, B. (2004). Serpentinization of oceanic peridotites: Implications for geochemical cycles and biological activity. In *The Subseafloor Biosphere at Mid-Ocean Ridges* (pp. 119–136). https://doi.org/10.1029/144GM08

Früh-Green, G. L., Orcutt, B. N., Green, S. L., Cotterill, C., Morgan, S., Akizawa, N., et al. (2017). Expedition 357 summary. *Proceedings of the International Ocean Discovery Program*, *357*. https://doi.org/10.14379/iodp.proc.357.101.2017

Früh-Green, G. L., Orcutt, B. N., Rouméjon, S., Lilley, M. D., Morono, Y., Cotterill, C., et al. (2018). Magmatism, serpentinization and life: Insights through drilling the Atlantis Massif (IODP Expedition 357). *Lithos*, *323*, 137–155. https://doi.org/10.1016/j.lithos.2018.09.012

Fullerton, K., Schrenk, M. O., Yucel, M., Manini, E., Marco, B., Rogers, T., et al. (2019). Plate tectonics drive deep biosphere microbial community structure. *EarthArXiv*. https://doi.org/10.31223/osf.io/gyr7n

German, C. R., & Von Damm, K. L. (2003). Hydrothermal Processes. In *Treatise on Geochemistry* (pp. 181–222). Cambridge: Cambridge University Press. https://doi.org/10.1017/CBO9781139084260.009

Glein, C. R., Baross, J. A., & Waite, J. H. (2015). The pH of Enceladus' ocean. *Geochimica et Cosmochimica Acta*, *162*, 202–219. https://doi.org/10.1016/j.gca.2015.04.017

Grossman, E. L., & Ku, T. L. (1986). Carbon and oxygen isotopic fractionation in biogenic aragonite-temp effects. *Chemical Geology*, *59*(April), 59–74. Retrieved from https://www.researchgate.net/publication/291049277

Hansell, D. A. (2002). *DOC in the Global Ocean Carbon Cycle*. *Biogeochemistry of Marine Dissolved Organic Matter*. Elsevier Inc. https://doi.org/10.1016/b978-012323841-2/50017-8

Hawkes, J. A., Rossel, P. E., Stubbins, A., Butterfield, D. A., Connelly, D. P., Achterberg, E. P., et al. (2015). Efficient removal of recalcitrant deep-ocean dissolved organic matter during hydrothermal circulation. *Nature Geoscience*, *8*(11), 856–860. https://doi.org/10.1038/ngeo2543

Hawkes, J. A., Hansen, C. T., Goldhammer, T., Bach, W., & Dittmar, T. (2016). Molecular alteration of marine dissolved organic matter under experimental hydrothermal conditions. *Geochimica et Cosmochimica Acta*, *175*, 68–85. https://doi.org/10.1016/j.gca.2015.11.025

Hendy, C. H. (1971). The isotopic geochemistry of speleothems-I. The calculation of the effects of different modes of formation on the isotopic composition of speleothems and their applicability as palaeoclimatic indicators. *Geochimica et Cosmochimica Acta*, *35*(8), 801–824. https://doi.org/10.1016/0016-7037(71)90127-X

Holm, N. G., Cairns-Smith, A. G., Daniel, R. M., Ferris, J. P., & Shock, E. L. (1992). Future Research. *Origins of Life and Evolution of the Biosphere*, *22*(1), 181–190.

Holm, N. G., Dumont, M., Ivarsson, M., & Konn, C. (2006). Alkaline fluid circulation in ultramafic rocks and formation of nucleotide constituents: A hypothesis. *Geochemical Transactions*, *7*, 14–16. https://doi.org/10.1186/1467-4866-7-7

Hu, B., Radke, J., Schlüter, H.-J., Heine, F. T., Zhou, L., & Bernasconi, S. M. (2014). A modified procedure for gas-source isotope ratio mass spectrometry: the long-integration dual-inlet (LIDI) methodology and implications for clumped isotope measurements. *Rapid Communications in Mass Spectrometry*, *28*(13), 1413–1425. https://doi.org/10.1002/rcm.6909

Jeffrey, L. M. (1969). *Development of a Method for Isolation of Gram Quantities of Dissolved Organic Matter from Seawater and Some Chemical and Isotopic Characteristics of the Isolated Materia*. Texas A&M University, College Station, TX.

Jones, R. M., Goordial, J. M., & Orcutt, B. N. (2018). Low energy subsurface environments as extraterrestrial analogs. *Frontiers in Microbiology*, *9*(JUL), 1–18. https://doi.org/10.3389/fmicb.2018.01605

Karson, J. A., Früh-Green, G. L., Kelley, D. S., Williams, E. A., Yoerger, D. R., & Jakuba, M. (2006). Detachment shear zone of the Atlantis Massif core complex, Mid-Atlantic Ridge, 30 °n. *Geochemistry, Geophysics, Geosystems*, *7*(6), n/a-n/a. https://doi.org/10.1029/2005GC001109

Kelemen, P. B., & Matter, J. M. (2008). In situ carbonation of peridotite for CO2 storage. *Proceedings of the National Academy of Sciences of the United States of America*, *105*(45), 17295–17300. https://doi.org/10.1073/pnas.0805794105

Kelemen, P. B., Matter, J. M., Streit, E. E., Rudge, J. F., Curry, W. B., & Blusztajn, J. S. (2011). Rates and Mechanisms of Mineral Carbonation in Peridotite: Natural Processes and Recipes for Enhanced, in situ CO 2 Capture and Storage. *Annual Review of Earth and Planetary Sciences*, *39*(1), 545–576. https://doi.org/10.1146/annurev-earth-092010-152509

Kelley, D. S. (1996). Methane-rich fluids in the oceanic crust. *Journal of Geophysical Research: Solid Earth*, *101*(B2), 2943–2962. https://doi.org/10.1029/95jb02252

Kelley, D. S., & Früh-Green, G. L. (1999). Abiogenic methane in deep-seated mid-ocean ridge environments: Insights from stable isotope analyses. *Journal of Geophysical Research: Solid Earth*, *104*(B5), 10439–10460. https://doi.org/10.1029/1999jb900058

Kelley, D. S., & Früh-Green, G. L. (2001). Volatile lines of descent in submarine plutonic environments: Insights from stable isotope and fluid inclusion analyses. *Geochimica et Cosmochimica Acta*, *65*(19), 3325–3346. https://doi.org/10.1016/S0016-7037(01)00667-6

Kelley, D. S., Karson, J. A., Blackman, D. K., Früh-Green, G. L., Butterfield, D. A., Lilley, M. D., et al. (2001). An off-axis hydrothermal vent field near the Mid-Atlantic Ridge at 30 degrees N. *Nature*, *412*(6843), 145–9. https://doi.org/10.1038/35084000

Kelley, D. S., Baross, J. A., & Delaney, J. R. (2002). Volcanoes, fluids, and life at mid-ocean ridge spreading centers. *Annual Review of Earth and Planetary Sciences*, *30*, 385–491. https://doi.org/10.1146/annurev.earth.30.091201.141331

Kelley, D. S., Karson, J. A., Früh-Green, G. L., Yoerger, D. R., Shank, T. M., Butterfield, D. A., et al. (2005). A Serpentinite-Hosted Ecosystem: The Lost City Hydrothermal Field. *Science*, *307*(5714), 1428–1434. https://doi.org/10.1126/science.1102556

Klein, F., Humphris, S. E., Guo, W., Schubotz, F., Schwarzenbach, E. M., Orsi, W. D., & Karl, D. M. (2015). Fluid mixing and the deep biosphere of a fossil Lost City-type hydrothermal system at the Iberia Margin. *Proceedings of the National Academy of Sciences of the United States of America*, *112*(39), 12036–12041. https://doi.org/10.1073/pnas.1504674112

Konn, C., Charlou, J. L., Holm, N. G., & Mousis, O. (2015). The production of methane, hydrogen, and organic compounds in ultramafic-hosted hydrothermal vents of the mid-atlantic ridge. *Astrobiology*, *15*(5), 381–399. https://doi.org/10.1089/ast.2014.1198

Kourkoumelis, N. (2013). PowDLL, a reusable .NET component for interconverting powder diffraction data: Recent developments. In L. O'Neill (Ed.), *ICDD Annual Spring Meetings* (Vol. 28, pp. 137–48).

Lafay, R., Baumgartner, L. P., Stephane, S., Suzanne, P., German, M. H., & Torsten, V. (2017). Petrologic and stable isotopic studies of a fossil hydrothermal system in ultramafic environment (Chenaillet ophicalcites, Western Alps, France): Processes of carbonate cementation. *Lithos*, *294–295*, 319–338. https://doi.org/10.1016/j.lithos.2017.10.006

Lafuente, B., Downs, R. T., Yang, H., & Stone, N. (2015). 1. The power of databases: The RRUFF project. In T. Armbruster & R. M. Danisi (Eds.), *Highlights in Mineralogical Crystallography* (pp. 1–30). Berlin, München, Boston: De Gruyter (O). https://doi.org/10.1515/9783110417104-003

Lang, S. Q., Butterfield, D. A., Lilley, M. D., Paul Johnson, H., & Hedges, J. I. (2006). Dissolved organic carbon in ridge-axis and ridge-flank hydrothermal systems. *Geochimica et Cosmochimica Acta*, *70*(15), 3830–3842. https://doi.org/10.1016/j.gca.2006.04.031

Lang, S. Q., Butterfield, D. A., Schulte, M. D., Kelley, D. S., & Lilley, M. D. (2010). Elevated concentrations of formate, acetate and dissolved organic carbon found at the Lost City hydrothermal field. *Geochimica et Cosmochimica Acta*, *74*(3), 941–952. https://doi.org/10.1016/j.gca.2009.10.045

Lang, S. Q., Früh-Green, G. L., Bernasconi, S. M., Lilley, M. D., Proskurowski, G., Méhay, S., & Butterfield, D. A. (2012). Microbial utilization of abiogenic carbon and hydrogen in a serpentinite-hosted system. *Geochimica et Cosmochimica Acta*, *92*, 82–99. https://doi.org/10.1016/j.gca.2012.06.006

Lang, S. Q., Früh-Green, G. L., Bernasconi, S. M., Brazelton, W. J., Schrenk, M. O., & McGonigle, J. M. (2018). Deeply-sourced formate fuels sulfate reducers but not methanogens at Lost City hydrothermal field. *Scientific Reports*, *8*(1), 1–10. https://doi.org/10.1038/s41598-017-19002-5

Lister, C. R. B. (1972). On the thermal balance of a mid-ocean ridge. *Geophys. J. R. Astron. Soc.*, *26*, 515–535.

Ludwig, K. A., Kelley, D. S., Butterfield, D. A., Nelson, B. K., & Früh-Green, G. L. (2006). Formation and evolution of carbonate chimneys at the Lost City Hydrothermal Field. *Geochimica et Cosmochimica Acta*, *70*(14), 3625–3645. https://doi.org/10.1016/j.gca.2006.04.016

Ludwig, K. A., Shen, C.-C., Kelley, D. S., Cheng, H., & Edwards, R. L. (2011). U-Th systematics and 230 Th ages of carbonate chimneys at the Lost City Hydrothermal Field. *Geochimica et Cosmochimica Acta*, *75*(7), 1869–1888. https://doi.org/10.1016/j.gca.2011.01.008

Martin, W. F., & Russell, M. J. (2007). On the origin of biochemistry at an alkaline hydrothermal vent. *Philosophical Transactions of the Royal Society B: Biological Sciences*, *362*(1486), 1887–1925. https://doi.org/10.1098/rstb.2006.1881

McCollom, T. M. (2013). Laboratory simulations of abiotic hydrocarbon formation in earth's deep subsurface. *Reviews in Mineralogy and Geochemistry*, *75*, 467–494. https://doi.org/10.2138/rmg.2013.75.15

McCollom, T. M., & Bach, W. (2009). Thermodynamic constraints on hydrogen generation during serpentinization of ultramafic rocks. *Geochimica et Cosmochimica Acta*, *73*(3), 856–875. https://doi.org/10.1016/j.gca.2008.10.032

McCollom, T. M., & Seewald, J. S. (2003). Experimental study of the hydrothermal reactivity of organic acids and acid anions: II. Acetic acid, acetate, and valeric acid. *Geochimica et Cosmochimica Acta*, *67*(19), 3645–3664. https://doi.org/10.1016/S0016-7037(03)00135-2

McCollom, T. M., & Seewald, J. S. (2007). Abiotic synthesis of organic compounds in deep-sea hydrothermal environments. *Chemical Reviews*, *107*(2), 382–401. https://doi.org/10.1021/cr0503660

McDermott, J. M., Seewald, J. S., German, C. R., & Sylva, S. P. (2015). Pathways for abiotic organic synthesis at submarine hydrothermal fields. *Proceedings of the National Academy of Sciences*, *112*(25), 7668–7672. https://doi.org/10.1073/pnas.1506295112

Meckler, A. N., Ziegler, M., Millán, M. I., Breitenbach, S. F. M., & Bernasconi, S. M. (2014). Long-term performance of the Kiel carbonate device with a new correction scheme for clumped isotope measurements. *Rapid Communications in Mass Spectrometry*, *28*(15), 1705–1715. https://doi.org/10.1002/rcm.6949

Ménez, B., Pasini, V., & Brunelli, D. (2012). Life in the hydrated suboceanic mantle. *Nature Geoscience*, *5*(2), 133–137. https://doi.org/10.1038/ngeo1359

Ménez, B., Pisapia, C., Andreani, M., Jamme, F., Vanbellingen, Q. P., Brunelle, A., et al. (2018). Abiotic synthesis of amino acids in the recesses of the oceanic lithosphere. *Nature*, *564*(7734), 59–63. https://doi.org/10.1038/s41586-018-0684-z

Motamedi, S., Orcutt, B. N., Früh-Green, G. L., Twing, K. I., Pendleton, H. L., & Brazelton, W. J. (2020). Microbial residents of the Atlantis Massif's shallow serpentinite subsurface. *Applied and Environmental Microbiology*, (March). https://doi.org/10.1128/AEM.00356-20

Mottl, M. J. (2003). Partitioning of energy and mass flux between midocean ridge axes and flanks at high and low temperature. *Energy and Mass Transfer in Marine Hydrothermal Systems*, 271–286.

Mottl, M. J., Komor, S. C., Fryer, P., & Moyer, C. L. (2003). Deep-slab fluids fuel extremophilic Archaea on a Mariana forearc serpentinite mud volcano: Ocean drilling program leg 195. *Geochemistry, Geophysics, Geosystems*, *4*(11), 1–14. https://doi.org/10.1029/2003GC000588

Müller, I. A., Fernández, Á., Radke, J., van Dijk, J., Bowen, D., Schwieters, J., & Bernasconi, S. M. (2017). Carbonate clumped isotope analyses with the long-integration dual-inlet (LIDI) workflow: scratching at the lower sample weight boundaries. *Rapid Communications in Mass Spectrometry*, *31*(12), 1057–1066. https://doi.org/10.1002/rcm.7878

Müller, I. A., Rodriguez-Blanco, J. D., Storck, J.-C., do Nascimento, G. S., Bontognali, T. R. R., Vasconcelos, C., et al. (2019). Calibration of the oxygen and clumped isotope thermometers for (proto-)dolomite based on synthetic and natural carbonates. *Chemical Geology*, *525*(December 2018), 1–17. https://doi.org/10.1016/j.chemgeo.2019.07.014

Neal, C., & Stanger, G. (1983). Hydrogen generation from mantle source rocks in Oman. *Earth and Planetary Science Letters*, *66*(C), 315–320. https://doi.org/10.1016/0012-821X(83)90144-9

Neal, C., & Stanger, G. (1985). Past And Present Serpentinisation of Ultramafic Rocks; An Example from the Semail Ophiolite Nappe of Northern Oman BT - The Chemistry of Weathering. In J. I. Drever (Ed.) (pp. 249–275). Dordrecht: Springer Netherlands. https://doi.org/10.1007/978-94-009-5333-8_15

Nooner, S. L., Sasagawa, G. S., Blackman, D. K., & Zumberge, M. A. (2003). Structure of oceanic core complexes: Constraints from seafloor gravity measurements made at the Atlantis Massif. *Geophysical Research Letters*, *30*(8), 8–11. https://doi.org/10.1029/2003GL017126

O'Neil, J. R., Clayton, R. N., & Mayeda, T. K. (1969). Oxygen isotope fractionation in divalent metal carbonates. *The Journal of Chemical Physics*, *51*(12), 5547–5558. https://doi.org/10.1063/1.1671982

Ohara, Y., Reagan, M. K., Fujikura, K., Watanabe, H., Michibayashi, K., Ishii, T., et al. (2012). A serpentinite-hosted ecosystem in the Southern Mariana Forearc. *Proceedings of the National Academy of Sciences of the United States of America*, *109*(8), 2831–5. https://doi.org/10.1073/pnas.1112005109

Orcutt, B. N., Sylvan, J. B., Knab, N. J., & Edwards, K. J. (2011). Microbial ecology of the dark ocean above, at, and below the seafloor. *Microbiology and Molecular Biology Reviews : MMBR*, *75*(2), 361–422. https://doi.org/10.1128/MMBR.00039-10

Palandri, J. L., & Reed, M. H. (2004). Geochemical models of metasomatism in ultramafic systems: Serpentinization, rodingitization, and sea floor carbonate chimney precipitation. *Geochimica et Cosmochimica Acta*, *68*(5), 1115–1133. https://doi.org/10.1016/j.gca.2003.08.006

Plümper, O., King, H. E., Geisler, T., Liu, Y., Pabst, S., Savov, I. P., et al. (2017). Subduction zone forearc serpentinites as incubators for deep microbial life. *Proceedings of the National Academy of Sciences*, *114*(17), 4324–4329. https://doi.org/10.1073/pnas.1612147114

Proskurowski, G., Lilley, M. D., Kelley, D. S., & Olson, E. J. (2006). Low temperature volatile production at the Lost City Hydrothermal Field, evidence from a hydrogen stable isotope geothermometer. *Chemical Geology*, *229*(4), 331–343. https://doi.org/10.1016/j.chemgeo.2005.11.005

Proskurowski, G., Lilley, M. D., Seewald, J. S., Früh-Green, G. L., Olson, E. J., Lupton, J. E., et al. (2008). Abiogenic Hydrocarbon Production at Lost City Hydrothermal Field. *Science*, *319*(5863), 604–607. https://doi.org/10.1126/science.1151194

Reimer, P. J., Brown, T. A., & Reimer, Ron, W. (2004). Discussion: Reporting and calibration of post-bomb 14C data. *Radiocarbon*, *46*(1), 1111–1150. Retrieved from http://scholar.google.com/scholar?hl=en&btnG=Search&q=intitle:Intcal09+and+Marine09+radiocarbon+age+calibration+curves,+0-50,000+years+cal+BP#0

Rossel, P. E., Stubbins, A., Rebling, T., Koschinsky, A., Hawkes, J. A., & Dittmar, T. (2017). Thermally altered marine dissolved organic matter in hydrothermal fluids. *Organic Geochemistry*, *110*, 73–86. https://doi.org/10.1016/j.orggeochem.2017.05.003

Rouméjon, S., Früh-Green, G. L., Orcutt, B. N., & IODP Expedition 357 Science Party. (2018). Alteration heterogeneities in peridotites exhumed on the southern wall of the Atlantis Massif (IODP Expedition 357). *Journal of Petrology*, *59*(7), 1329–1358. https://doi.org/10.1093/petrology/egy065

Rouméjon, S., Williams, M. J., & Früh-Green, G. L. (2018). In-situ oxygen isotope analyses in serpentine minerals: Constraints on serpentinization during tectonic exhumation at slow- and ultraslow-spreading ridges. *Lithos*, *323*, 156–173. https://doi.org/10.1016/j.lithos.2018.09.021

Ruff, M., Szidat, S., Gäggeler, H. W., Suter, M., Synal, H. A., & Wacker, L. (2010). Gaseous radiocarbon measurements of small samples. *Nuclear Instruments and Methods in Physics Research, Section B: Beam Interactions with Materials and Atoms*, *268*(7–8), 790–794. https://doi.org/10.1016/j.nimb.2009.10.032

Schrag, D. P., Adkins, J. F., McIntyre, K., Alexander, J. L., Hodell, D. A., Charles, C. D., & McManus, J. F. (2002). The oxygen isotopic composition of seawater during the Last Glacial Maximum. *Quaternary Science Reviews*, *21*(1–3), 331–342. https://doi.org/10.1016/S0277-3791(01)00110-X

Schrenk, M. O., Kelley, D. S., Bolton, S. A., & Baross, J. A. (2004). Low archaeal diversity linked to subseafloor geochemical processes at the Lost City Hydrothermal Field, Mid-Atlantic Ridge. *Environmental Microbiology*, *6*(10), 1086–1095. https://doi.org/10.1111/j.1462-2920.2004.00650.x

Schrenk, M. O., Brazelton, W. J., & Lang, S. Q. (2013). Serpentinization, carbon, and deep life. *Reviews in Mineralogy and Geochemistry*, *75*, 575–606. https://doi.org/10.2138/rmg.2013.75.18

Schroeder, T. J., & John, B. E. (2004). Strain localization on an oceanic detachment fault system, Atlantis Massif, 30°N, Mid-Atlantic Ridge. *Geochemistry, Geophysics, Geosystems*, *5*(11). https://doi.org/10.1029/2004GC000728

Schroeder, T. J., John, B. E., & Frost, R. B. (2002). Geologic implications of seawater circulation through peridotite exposed at slow-spreading mid-ocean ridges. *Geology*, *30*(4), 367–370.

Schwarzenbach, E. M., Früh-Green, G. L., Bernasconi, S. M., Alt, J. C., & Plas, A. (2013). Serpentinization and carbon sequestration: A study of two ancient peridotite-hosted hydrothermal systems. *Chemical Geology*, *351*, 115–133. https://doi.org/10.1016/j.chemgeo.2013.05.016

Seewald, J. S. (2001). Aqueous geochemistry of low molecular weight hydrocarbons at elevated temperatures and pressures: Constraints from mineral buffered laboratory experiments. *Geochimica et Cosmochimica Acta*, *65*(10), 1641–1664. https://doi.org/10.1016/S0016-7037(01)00544-0

Seifritz, W. (1990). CO2 disposal by means of silicates. *Nature*, *345*(June), 1990.

Sekine, Y., Shibuya, T., Postberg, F., Hsu, H. W., Suzuki, K., Masaki, Y., et al. (2015). High-temperature water-rock interactions and hydrothermal environments in the chondrite-like core of Enceladus. *Nature Communications*, *6*. https://doi.org/10.1038/ncomms9604

Seyfried, W. E., Pester, N. J., Tutolo, B. M., & Ding, K. (2015). The Lost City hydrothermal system: Constraints imposed by vent fluid chemistry and reaction path models on subseafloor heat and mass transfer processes. *Geochimica et Cosmochimica Acta*, *163*, 59–79. https://doi.org/10.1016/j.gca.2015.04.040

Shanks, W. C., Böhlke, J. K., & Seal, R. R. (1995). Stable isotopes in mid-ocean ridge hydrothermal systems: interactions between fluids, minerals, and organisms. *SeaBoor Hydrothermal Systems: Physical, Chemical, Biological, and Geological Interactions*, *70*, 194–221.

Shock, E. L. (1990). Geochemical constraints on the origin of organic compounds in hydrothermal systems. *Origins of Life and Evolution of the Biosphere*, *20*(3–4), 331–367. https://doi.org/10.1007/BF01808115

Shock, E. L., & Schulte, M. D. (1998). Organic synthesis during fluid mixing in hydrothermal systems. *Journal of Geophysical Research: Planets*, *103*(E12), 28513–28527. https://doi.org/10.1029/98JE02142

Staudigel, H., Hart, S. R., Schmincke, H. U., & Smith, B. M. (1989). Cretaceous ocean crust at DSDP Sites 417 and 418: Carbon uptake from weathering versus loss by magmatic outgassing. *Geochimica et Cosmochimica Acta*, *53*(11), 3091–3094. https://doi.org/10.1016/0016-7037(89)90189-0

Synal, H. A., Stocker, M., & Suter, M. (2007). MICADAS: A new compact radiocarbon AMS system. *Nuclear Instruments and Methods in Physics Research, Section B: Beam Interactions with Materials and Atoms*, *259*(1), 7–13. https://doi.org/10.1016/j.nimb.2007.01.138

Szatmari, P. (1989). Petroleum Formation by Fischer-Tropsch Synthesis in Plate Tectonics. *AAPG Bulletin*, *73*(8), 989–998. https://doi.org/10.1306/44B4A2CB-170A-11D7-8645000102C1865D

Takai, K., Nakamura, K., Toki, T., Tsunogai, U., Miyazaki, M., Miyazaki, J., et al. (2008). Cell proliferation at 122°C and isotopically heavy CH4 production by a hyperthermophilic methanogen under high-pressure cultivation. *Proceedings of the National Academy of Sciences of the United States of America*, *105*(31), 10949–10954. https://doi.org/10.1073/pnas.0712334105

Thayer, T. P. (1966). Serpentinization considered as a constant volume metasomatic process: *The American Mineralogist*, *51*, 685–710. Retrieved from http://scholar.google.com/scholar?hl=en&btnG=Search&q=intitle:Serpentinization+considered+as+a+constant+volume+metasomatic+process:+A+discussion#0

Wacker, L., Bonani, G., Friedrich, M., Hajdas, I., Kromer, B., Němec, M., et al. (2010). Micadas: Routine and high-precision radiocarbon dating. *Radiocarbon*, *52*(2), 252–262. https://doi.org/10.1017/S0033822200045288

Welhan, J. A. (1988). Origins of methane in hydrothermal systems. *Chemical Geology*, *71*(1–3), 183–198. https://doi.org/10.1016/0009-2541(88)90114-3

Welhan, J. A., & Craig, H. (1979). Methane and Hydrogen in East Pacific Rise Hydrothermal Fluids. *Geophysical Research Letters*, *6*(11), 829–831.

Wheat, C. G., & Mottl, M. J. (2004). Geochemical fluxes through mid-ocean ridge flanks. *In Hydrogeology of the Oceanic Lithosphere*, 627–658.

Zeebe, R. E., & Wolf-Gladrow, D. (2001). *CO2 in Seawater: Equilibrium, Kinetics, Isotopes*. *Elsevier Oceanography Series 65*. Elsevier.

Zhang, T., Ellis, G. S., Wang, K., Walters, C. C., Kelemen, S. R., Gillaizeau, B., & Tang, Y. (2007). Effect of hydrocarbon type on thermochemical sulfate reduction. *Organic Geochemistry*, *38*(6), 897–910. https://doi.org/10.1016/j.orggeochem.2007.02.004